

# Direct observations of electron firehose fluctuations in the magnetic reconnection outflow

Giulia Cozzani<sup>1</sup>, Yuri V. Khotyaintsev<sup>2</sup>, Daniel Bruce Graham<sup>2</sup>, and Mats André<sup>2</sup>

<sup>1</sup>University of Helsinki

<sup>2</sup>Swedish Institute of Space Physics

December 7, 2022

## Abstract

Electron temperature anisotropy-driven instabilities such as the electron firehose instability (EFI) are especially significant in space collisionless plasmas, where collisions are so scarce that wave-particle interactions are the leading mechanisms in the isotropization of the distribution function and energy transfer. Observational statistical studies provided convincing evidence in favor of the EFI constraining the electron distribution function and limiting the electron temperature anisotropy. Magnetic reconnection is characterized by regions of enhanced temperature anisotropy that could drive instabilities – including the electron firehose instability – affecting the particle dynamics and the energy conversion. However, in situ observations of the fluctuations generated by the EFI are still lacking and the interplay between magnetic reconnection and EFI is still largely unknown. In this study, we use high-resolution in situ measurements by the Magnetospheric Multiscale (MMS) spacecraft to identify and investigate EFI fluctuations in the magnetic reconnection exhaust in the Earth’s magnetotail. We find that the wave properties of the observed fluctuations largely agree with theoretical predictions of the non-propagating EF mode. These findings are further supported by comparison with the linear kinetic dispersion relation. Our results demonstrate that the magnetic reconnection outflow can be the seedbed of EFI and provide the first direct in situ observations of EFI-generated fluctuations.

# Direct observations of electron firehose fluctuations in the magnetic reconnection outflow

G. Cozzani<sup>1,2</sup>, Yu. V. Khotyaintsev<sup>2</sup>, D. B. Graham<sup>2</sup>, M. André<sup>2</sup>

<sup>1</sup>Department of Physics, University of Helsinki, Helsinki, Finland

<sup>2</sup>Swedish Institute of Space Physics, Uppsala, Sweden

## Key Points:

- Magnetic reconnection exhausts host regions of enhanced electron temperature anisotropy where the electron firehose instability can develop
- We analyze waves associated with regions where the electron firehose instability (EFI) threshold is exceeded
- We report direct in situ observations of the non-propagating electron firehose wave mode in the magnetic outflow region in the magnetotail

---

Corresponding author: G. Cozzani, [giulia.cozzani@helsinki.fi](mailto:giulia.cozzani@helsinki.fi)

Corresponding author: Yu. V. Khotyaintsev, [yuri@irfu.se](mailto:yuri@irfu.se)

**Abstract**

Electron temperature anisotropy-driven instabilities such as the electron firehose instability (EFI) are especially significant in space collisionless plasmas, where collisions are so scarce that wave-particle interactions are the leading mechanisms in the isotropization of the distribution function and energy transfer. Observational statistical studies provided convincing evidence in favor of the EFI constraining the electron distribution function and limiting the electron temperature anisotropy. Magnetic reconnection is characterized by regions of enhanced temperature anisotropy that could drive instabilities – including the electron firehose instability – affecting the particle dynamics and the energy conversion. However, in situ observations of the fluctuations generated by the EFI are still lacking and the interplay between magnetic reconnection and EFI is still largely unknown. In this study, we use high-resolution in situ measurements by the Magnetospheric Multiscale (MMS) spacecraft to identify and investigate EFI fluctuations in the magnetic reconnection exhaust in the Earth’s magnetotail. We find that the wave properties of the observed fluctuations largely agree with theoretical predictions of the non-propagating EF mode. These findings are further supported by comparison with the linear kinetic dispersion relation. Our results demonstrate that the magnetic reconnection outflow can be the seedbed of EFI and provide the first direct in situ observations of EFI-generated fluctuations.

**Plain Language Summary**

Space and astrophysical plasmas can be often treated as collisionless since they are sufficiently tenuous and warm and particle-particle collisions can be neglected. Because of the scarcity of particle-particle collisions, the local thermodynamics equilibrium is generally not established and collisionless processes play a key role in energy conversion and heating. As local thermodynamic equilibrium is not achieved, particle distribution functions can significantly depart from Maxwellian distribution functions, leading to the development of instabilities and the formation of waves. This study focus in particular on the electron firehose instability (EFI). It is established that the EFI constraints the electron distribution function but direct observations of the waves generated by EFI are still lacking. In this study, we use high-cadence spacecraft observations by the Magnetospheric MultiScale (MMS) spacecraft mission to identify and investigate waves generated by the EFI. We will focus on EFI observations during a magnetic reconnection event in the Earth’s magnetotail. Magnetic reconnection is a fundamental process of energy conversion in collisionless plasmas and investigating the interplay between magnetic reconnection and instability such as the EFI is critical to fully understanding energy conversion in plasmas. Our results provide the first direct observations of waves generated by the EFI.

**1 Introduction**

Kinetic plasma instabilities driven by temperature anisotropies are known to play an essential role in collisionless plasma dynamics, scattering the particles and affecting particle heating and energy conversion between the electromagnetic fields and particles (e.g., Gary, 1993). Among these anisotropy-driven instabilities, the whistler anisotropy instability is excited by electron temperature anisotropy  $T_{e,\parallel}/T_{e,\perp} < 1$  while the electron firehose instability (EFI) develops if  $T_{e,\parallel}/T_{e,\perp} > 1$ , where  $T_{e,\parallel}$  and  $T_{e,\perp}$  are the electron temperatures respectively parallel and perpendicular with respect to the background magnetic field. The EFI is believed to constrain the electron temperature anisotropy by inducing heating (cooling) in the perpendicular (parallel) direction with respect to the background magnetic field, thus leading to isotropization.

The EFI was described for the first time by Hollweg and Völk (1970) and W. Pilipp and Völk (1971). Then, Gary and Madland (1985) provided the parametric dependencies of the growth rate of the EF modes with the assumption of parallel propagation, i.e.

63 the wave vector  $\mathbf{k}$  is directed parallel to the background magnetic field. One-dimensional  
 64 Particle-In-Cell (PIC) simulations further investigated the properties of the parallel prop-  
 65 agating EF mode (Messmer, P., 2002; Paesold, G. & Benz, A. O., 2003). However, stud-  
 66 ies using both analytical and numerical approaches demonstrated the presence of two  
 67 distinct branches of the EFI (Gary & Nishimura, 2003; Li & Habbal, 2000; Campore-  
 68 ale & Burgess, 2008; Hellinger et al., 2014). These studies are based on linear theory and  
 69 2D PIC simulations. In particular, the linear kinetic dispersion theory predicts a prop-  
 70 agating EF mode characterized by parallel propagation with respect to the background  
 71 magnetic field, and a non-propagating EF mode predicted to develop for oblique wave-  
 72 normal angles. In addition, the non-propagating EF mode is resonant with both ions and  
 73 electrons, while the propagating EF mode is non-resonant with respect to electrons. The  
 74 two EF modes have been labeled in different ways, depending on the characteristics that  
 75 the different studies wanted to highlight. In this paper, we chose to refer to the two modes  
 76 as non-propagating and propagating EF modes, similar to Camporeale and Burgess (2008).  
 77 The former is called also oblique, resonant, and a-periodic mode in other studies; the lat-  
 78 ter is called parallel, non-resonant and periodic (Li & Habbal, 2000; Gary & Nishimura,  
 79 2003; López et al., 2022).

80 There is a consensus that the non-propagating (oblique, resonant) mode is char-  
 81 acterized by a lower threshold and higher growth rate compared with the propagating  
 82 (parallel, non-resonant) mode. Hence, in this study, we will focus exclusively on the non-  
 83 propagating EF mode as it is expected to be more efficient than the propagating EF mode  
 84 in constraining the electron temperature anisotropy. The properties of the EF modes will  
 85 be presented in detail in Section 2, focusing in particular on the non-propagating EF mode.

86 In the past decades, the electron firehose instability has been investigated in par-  
 87 ticular in the context of solar wind plasmas (Verscharen et al., 2022, and references therein)  
 88 since the EFI is invoked as one of the most significant possible isotropization mechanisms  
 89 to explain the quasi-isotropic state of the solar wind electrons. Indeed, the electron dis-  
 90 tribution functions observed in the solar wind are much closer to isotropic distributions  
 91 than expected by considering the Chew–Goldberger–Low (CGL) model (Chew et al., 1956)  
 92 of a spherically expanding solar wind (Štverák et al., 2008). Hence, the development of  
 93 temperature-anisotropy-driven instabilities could explain the discrepancy between the  
 94 model and the observed quasi-isotropic electron distributions. Statistical observational  
 95 studies have confirmed the scenario of the EFI being crucial for isotropization by show-  
 96 ing that the temperature anisotropy is well constrained by the thresholds of temperature-  
 97 anisotropy-driven instabilities, notably the whistler instability and the EFI (Štverák et  
 98 al., 2008; Cattell et al., 2022). Recently, several studies were devoted to investigating the  
 99 EFI by modeling the solar wind electron distribution with more accuracy (both focus-  
 100 ing on the propagating EF mode only (Lazar et al., 2016; Shaaban et al., 2021) or in-  
 101 cluding also the non-propagating mode (Shaaban et al., 2019)). This includes going be-  
 102 yond the bi-Maxwellian approximation and taking into account the complex structure  
 103 of the solar wind electron distribution function – consisting of a thermal core, a suprather-  
 104 mal halo, and a field-aligned beam (Feldman et al., 1975; W. G. Pilipp et al., 1987). Other  
 105 efforts have been devoted to the investigation of the EFI onset (Innocenti et al., 2019)  
 106 and evolution (Camporeale & Burgess, 2008; Hellinger et al., 2014; Innocenti et al., 2019).  
 107 These studies focus on the non-propagating EF mode, as it arises self-consistently in the  
 108 simulations of expanding solar wind (Innocenti et al., 2019) and has the larger growth  
 109 rate in all simulations, consistently with the predictions of the linear theory.

110 Despite the majority of the work having been devoted to the study of the EFI in  
 111 the solar wind context, the EFI can arise in any space environment where the plasma  
 112 is unstable to the instability. Statistical studies collected and analyzed electron distri-  
 113 bution functions in different near-Earth plasmas. Gary et al. (2005) used Cluster data  
 114 to investigate electron distributions in the magnetosheath, while Zhang et al. (2018) used  
 115 THEMIS observations to study electron distributions at dipolarization fronts in the mag-

116 netotail. These studies show that the electron distribution functions are constrained by  
 117 the EFI threshold, suggesting that the EFI plays an important role in shaping the dis-  
 118 tribution functions.

119 Magnetic reconnection is a fundamental plasma process that plays a key role in en-  
 120 ergy conversion, plasma heating, and particle energization in a variety of plasma envi-  
 121 ronments (Biskamp, 2000). The magnetic reconnection process is characterized by re-  
 122 gions of enhanced temperature anisotropy (Egedal et al., 2013) that can be the seedbed  
 123 for temperature anisotropy-driven instabilities. Indeed, a 3D PIC simulation study re-  
 124 cently reported the presence of EFI-generated fluctuations in the reconnection outflow  
 125 region (Le et al., 2019). The particle scattering and wave-particle interaction processes  
 126 induced by the development of the EFI could potentially affect the energy conversion  
 127 and acceleration produced by the reconnection process. However, little is known about  
 128 the interplay between magnetic reconnection and the EFI. More importantly, direct ob-  
 129 servations of the EFI-generated fluctuations are currently lacking.

130 In previous studies focusing on near-Earth plasmas the presence of the EFI has been  
 131 detected somewhat *indirectly* by looking at the limited anisotropy of the electron dis-  
 132 tribution functions (Zhang et al., 2018; Gary et al., 2005). The effect of the EFI is com-  
 133 monly inferred from the fact that the electron distribution is bounded by the instabil-  
 134 ity threshold. This approach is suitable for statistical studies but it does not allow for  
 135 *direct* observations of the EF wave modes. In this study, we use high-resolution measure-  
 136 ments of the Magnetospheric Multiscale mission (MMS) (Burch et al., 2016) to shed light  
 137 on the EFI-generated waves in the Earth’s magnetotail. We report MMS observations  
 138 of the non-propagating EF mode in the magnetic reconnection outflow region observed  
 139 by MMS during a current sheet flapping event in the magnetotail. We show that the ob-  
 140 served electron temperature anisotropy is constrained by the EFI threshold and we present  
 141 *direct* in situ observations of the EFI-generated fluctuations.

142 This paper is organized as follows: In Section 2, we review the properties of the EF  
 143 modes based on linear dispersion theory, focusing in particular on the non-propagating  
 144 EF mode. In Section 3, we introduce the MMS data products used in this study. In Sec-  
 145 tion 4, we present an overview of the current sheet flapping event in the Earth’s mag-  
 146 netotail that we used for the analysis and we discuss the selection criteria for the EF events.  
 147 Then, we present the detailed analysis of the EF fluctuations observed during two of the  
 148 selected EF events in Section 5. In Section 6 we compare the results of the in situ space-  
 149 craft observations with a numerical solver. Sections 8 and 9 present the discussion and  
 150 the conclusions respectively.

## 151 2 Properties of Electron Firehose Modes

152 Linear kinetic dispersion theory predicts that a magnetized plasma can be unsta-  
 153 ble to the development of the EFI under the condition of presenting a sufficiently large  
 154 electron temperature anisotropy and being sufficiently warm, i.e. with  $\beta_{e,\parallel} > 2$  ( $\beta_{e,\parallel} =$   
 155  $2\mu_0 n_e T_{e,\parallel} / B^2$ , where  $\mu_0$  is the vacuum magnetic permeability,  $n_e$  is the electron num-  
 156 ber density and  $B$  is the ambient magnetic field). As mentioned in the Introduction, the  
 157 linear theory predicts the presence of two distinct branches of the EFI. One is propa-  
 158 gating (real frequency  $\omega \neq 0$ ) and it is characterized by parallel propagation at small  
 159  $\theta_{kB}$  (where  $\theta_{kB}$  is the angle between the wave vector  $\mathbf{k}$  and the background magnetic field);  
 160 the other mode is non-propagating and predicted to develop for oblique wave-normal an-  
 161 gles,  $\theta_{kB}$ . For  $\theta_{kB} > 30^\circ$  the mode was defined as oblique by several studies (Li & Hab-  
 162 bal, 2000; Gary & Nishimura, 2003), while more recently Camporeale and Burgess (2008)  
 163 considered a higher threshold of  $\theta_{kB} \sim 50^\circ$  to discriminate between the parallel and oblique  
 164 mode.

165 It is established by both analytical and numerical studies that the non-propagating  
 166 (oblique, resonant) mode is characterized by a lower threshold and higher growth rate  
 167 than the propagating (parallel, non-resonant) mode. Indeed, the growth rate  $\gamma$  of the  
 168 non-propagating mode is expected to be  $\Omega_{ci} < \gamma < \Omega_{ce}$ , while  $\gamma < \Omega_{ci}$  for the propa-  
 169 gating mode (Gary & Nishimura, 2003) (here  $\Omega_\alpha = eB/m_\alpha$  is the cyclotron frequency,  
 170  $e$  the elementary charge and  $m_\alpha$  the mass,  $\alpha = e, i$  indicates the electron and ion species).  
 171 For this reason, in the following, we will focus on the non-propagating EF mode only.

172 The EF instability threshold is predicted by the linear dispersion theory. The thresh-  
 173 old depends upon the electron temperature anisotropy  $T_{e,\parallel}/T_{e,\perp}$  and the parallel elec-  
 174 tron beta  $\beta_{e,\parallel}$  and in the following we will use to formulation reported by Gary and Nishimura  
 175 (2003), which reads

$$\frac{T_{e,\parallel}}{T_{e,\perp}} = \frac{1}{1 - S'_e/\beta_{e,\parallel}^{\alpha'_e}}. \quad (1)$$

176 The two primed quantities are dimensionless fitting parameters with  $1 \lesssim S'_e \lesssim$   
 177  $2$  and  $\alpha'_e \lesssim 1$  which are defined for  $2 \leq \beta_{e,\parallel} \leq 50$ . For an instability growth rate  $\gamma/\Omega_{ce} =$   
 178  $0.001$ ,  $S'_e = 1.29$  and  $\alpha'_e = 0.97$ .

179 The non-propagating EF mode is resonant with both ions and electrons. To estab-  
 180 lish if a mode is resonant or non-resonant with a plasma species, one can evaluate the  
 181 Landau resonance factor  $\zeta_\alpha = \omega/\sqrt{2}|k_\parallel|v_{th,\alpha}$  and the cyclotron resonance factor  $\zeta_\alpha^\pm =$   
 182  $|\omega \pm \Omega_{c\alpha}|/\sqrt{2}|k_\parallel|v_{th,\alpha}$ . Here,  $|k_\parallel|$  is the magnitude of the wave vector compo-  
 183 nent parallel to the background magnetic field and  $v_{th,\alpha}$  is the thermal speed. In particular, for  
 184 resonant species, which strongly interact with the waves, the resonant velocity is expected  
 185 to lay within a thermal speed of the distribution function peak, satisfying the condition  
 186  $\zeta_\alpha, \zeta_\alpha^\pm \lesssim 1$ . Instead, for non-resonant species  $\zeta_\alpha, \zeta_\alpha^\pm \gg 1$  (Gary et al., 1984). For a  
 187 non-propagating mode, the Landau resonant factor is  $Re(\zeta_\alpha) = 0$ .

188 Figure 1 shows the properties of the non-propagating EF mode for  $\beta_{e,\parallel} = 9$  and  
 189  $T_{e,\parallel}/T_{e,\perp} = 2$ . The value of  $\beta_{e,\parallel} = 9$  is representative of the magnetotail plasma sheet  
 190 conditions. Figure 1 is obtained with the numerical solver Plasma Dispersion Relation  
 191 Kinetics (PDRK, (Xie & Xiao, 2016)) which solves the kinetic linear dispersion relation  
 192 for multi-species plasmas in the magnetized electromagnetic case. The model implemented  
 193 in the solver assumes that the plasma density is homogeneous, as well as the background  
 194 magnetic field. The properties are shown in the parameter space composed of the nor-  
 195 malized wave vector  $k\rho_e$  and the wave-normal angle  $\theta_{kB}$  ( $\rho_e$  is the electron Larmor ra-  
 196 dius). Figure 1(a) shows that this choice of input parameters leads to positive growth  
 197 with a maximum rate  $\gamma_{max}/\Omega_{ce} \sim 0.13$ . A positive growth rate is found for  $k\rho_e \lesssim 1$   
 198 and the wave vector at maximum  $\gamma = \gamma_{max}$  is  $k\rho_e = 0.66$ . As discussed above, the  
 199 non-propagating EF mode is associated with oblique wave-normal angle  $\theta_{kB}$  and, for the  
 200 chosen set of parameters, the wave-normal angle at the maximum growth rate is  $\theta_{kB} =$   
 201  $69^\circ$  (see Fig.1(a)). Figure 1(b) confirms that the mode is non-propagating, as  $\omega = 0$   
 202 in all points of the parameter space. To quantify the waves electrostatic and electromag-  
 203 netic components we use the parameter  $\mathcal{E}_{long} = |\mathbf{E} \cdot \hat{\mathbf{k}}|^2/|\mathbf{E}|^2$  which is equal to 1 for a  
 204 purely longitudinal electrostatic wave and equal to 0 for a transverse electromagnetic wave.  
 205 Figure 1(c) shows that  $\mathcal{E}_{long} < 0.5$  in the region of significant positive growth rate mean-  
 206 ing that the non-propagating EF mode is electromagnetic. In Figure 1(d) we show the  
 207 ratio  $\delta B_\parallel/\delta B$  where  $\delta B_\parallel$  is the fluctuating magnetic field parallel to the background mag-  
 208 netic field and  $\delta B$  is the total fluctuating magnetic field. The magnetic field fluctuations  
 209 are predominantly transverse i.e.  $|\delta B_\perp|^2 \gg |\delta B_\parallel|^2$ . The  $\delta E_\parallel/\delta E$  ratio (Fig. 1(e)) in-  
 210 dicates that the electric field fluctuations are dominated by the component aligned with  
 211 the background magnetic field. Then, Figure 1(f) shows the polarization of the electric  
 212 field fluctuations. For non-propagating waves, the polarization can be defined as  $P =$   
 213  $i\frac{\delta E_x}{\delta E_y}$ , where  $\delta E_x$  and  $\delta E_y$  are two components of the electric field fluctuations. In the solver,

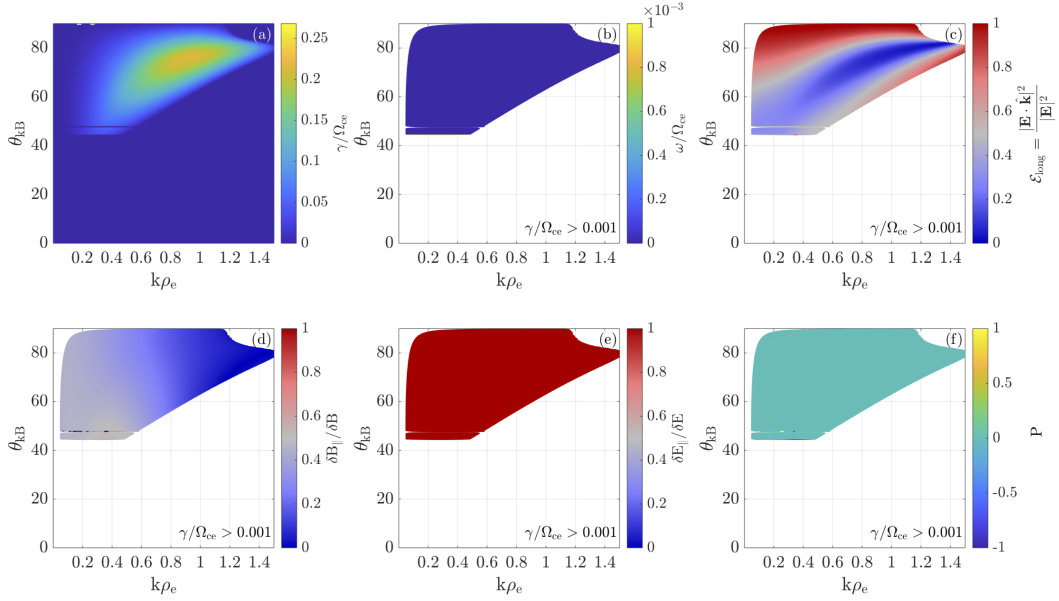


**Figure 1.** Properties of the non-propagating EF mode computed with the PDRK numerical solver. The input parameters used in the numerical solver are  $T_{e,\parallel} = 1000$  eV,  $T_{e,\perp} = 500$  eV, the background magnetic field  $B = 3$  nT and density  $n_e = n_i = n = 0.2 \text{ cm}^{-3}$  while the isotropic ion temperature is  $T_i = T_{i,\parallel} = T_{i,\perp} = 4000$  eV. The panels show the parameters space  $k\rho_e$ – $\theta_{kB}$  versus (a) imaginary frequency  $\gamma/\Omega_{ce}$  (b) real frequency  $\omega/\Omega_{ce}$  (c)  $\mathcal{E}_{\text{long}} = |\mathbf{E} \cdot \hat{\mathbf{k}}|^2/|\mathbf{E}|^2$  (d)  $\delta B_{\parallel}/\delta B$  (e)  $\delta E_{\parallel}/\delta E$  (f) polarization  $P = i \frac{\delta E_x}{\delta E_y}$ . The quantities in panels (b)–(f) are shown for values of the growth rate exceeding the marginal stability condition, which is usually set at  $10^{-3}$  (Camporeale & Burgess, 2008).

214 the background magnetic field is along the  $z$  direction while the wave vector  $\mathbf{k} = (k_x, 0, k_z)$ .  
 215 As the polarization is 0 for all the values of  $k\rho_e$  and  $\theta_{kB}$  in Fig.1(f), the waves are ex-  
 216 pected to have a linear polarization.

217 In Section 5 we will consider several of the characteristics discussed above to identifi-  
 218 fy fluctuations consistent with the non-propagating EF mode in MMS in situ obser-  
 219 vations. In particular, EFI-generated waves are expected to have zero real frequency and  
 220 a wave vector  $k\rho_e \lesssim 1$  directed obliquely with respect to the background magnetic field.  
 221 The fluctuations are also expected to have a significant electromagnetic component (quan-  
 222 tified via  $\mathcal{E}_{\text{long}}$ ) and to be resonant with electrons.

### 223 3 Magnetospheric MultiScale (MMS) Data

224 We use data from the Magnetospheric MultiScale (MMS) spacecraft (Burch et al.,  
 225 2016). In particular, we use the magnetic field  $\mathbf{B}$  data from the fluxgate magnetometer  
 226 (FGM) (Russell et al., 2016), electric field data  $\mathbf{E}$  from the spin-plane double probes (SDP)  
 227 (Lindqvist et al., 2016) and the axial double probe (ADP) (Ergun et al., 2016), and parti-  
 228 cle data from the fast plasma investigation (FPI) (Pollock et al., 2016). All data pre-  
 229 sented in this paper are high-resolution burst mode data. During the time interval sel-  
 230 lected for this study (15:24:00.0–15:58:00.0 UTC on 2017-07-06), the spacecraft were in  
 231 a tetrahedral configuration with inter-spacecraft separation of  $\sim 16$  km. In the interval  
 232 of interest, the average electron inertial length is 14 km, so the inter-spacecraft separa-

233 tion is comparable with the electron scales. Data from the MMS1 spacecraft are shown  
 234 throughout the paper, as the observations are similar for the four spacecraft.

#### 235 4 Event Overview and Data Selection

236 We consider a 34-minutes-long interval on 2017-07-06 when MMS was located at  
 237  $[-24.1, 1.5, 4.4] R_E$  (in Geocentric Solar Magnetospheric GSM coordinate system) in  
 238 the Earth's magnetotail. During this interval, MMS observes multiple crossings of the  
 239 magnetotail current sheet, identified by the frequent  $B_x$  reversals (see Fig.2(a)). The plasma  
 240 density (see Fig.2(c)) shows variations that are associated with the magnetic field. Higher  
 241 values of the magnetic field (e.g.  $|B| \sim 20$  nT at 15:40:02.7) correspond to lower den-  
 242 sities ( $n \sim 0.1$  cm $^{-3}$ ), indicating that MMS is sampling the lobe region, while lower val-  
 243 ues of magnetic field (e.g.  $|B| \sim 1.5$  nT at 15:40:50.0) are associated with higher den-  
 244 sities in the plasma sheet ( $n \sim 0.26$  cm $^{-3}$ ). These observations indicate that the cur-  
 245 rent sheet is flapping (e.g. Richard et al., 2021; Gao et al., 2018). During this interval,  
 246 MMS often observes fast plasma flows. As shown in Fig.2(b), the x component of the  
 247 ion velocity reaches values of  $|V_{i,x}| \sim 1000$  km/s. The highest values are observed close  
 248 to the neutral line  $B_x \sim 0$  while the value of  $V_{i,x}$  decreases toward zero when  $B_x$  in-  
 249 creases which corresponds to MMS entering the lobe region. In the first part of the in-  
 250 terval,  $V_{i,x} < 0$  so the flow is directed tailward. At  $\sim 15:46:41$  MMS observes a flow re-  
 251 versal followed by strong Earthward flow with  $V_{i,x} \sim 1000$  km/s. The observed flow  
 252 characteristics suggest that MMS is sampling the magnetic reconnection outflow region,  
 253 tailward outflow first and then Earthward flow. Similar conclusions were drawn in a study  
 254 by Leonenko et al. (2021) focusing on the properties of super thin current sheets (sub-  
 255 ion scale thickness) observed during the flapping event. We conclude that MMS observed  
 256 a tailward retreating X-line in the magnetotail.

257 As the main goal of this study is the investigation of the EFI and the associated  
 258 waves, we compute the instability threshold in order to identify the intervals in which  
 259 the instability could develop. Figure 2(d) and 2(e) shows that there are several data points  
 260 where  $T_{e,\parallel}/T_{e,\perp} > 1$  and  $\beta_{e,\parallel} > 2$  at the same time, which is a necessary condition  
 261 for the development of the EFI. Then, Figure 2(f) shows the quantity  $\mathcal{T}_{\text{EFI}} = \frac{T_{e,\parallel}}{T_{e,\perp}} - (1 -$   
 262  $S'_e/\beta_{e,\parallel}^{\alpha'_e})^{-1}$  which is obtained recasting Eq. 1. If  $\mathcal{T}_{\text{EFI}} > 0$  the threshold for the firehose  
 263 instability is exceeded and the generation of waves is expected. We find 24 intervals with  
 264  $\mathcal{T}_{\text{EFI}} > 0$ . Two time points  $t_1$  and  $t_2$  for which  $\mathcal{T}_{\text{EFI}} > 0$  are considered to be part of  
 265 the same interval if  $t_2 - t_1 < \tau$  where  $\tau = 0.3$  s. This value of  $\tau$  corresponds to sub-  
 266 ion time scales. In particular, it corresponds to one-third of an ion time scale computed  
 267 considering a typical ion bulk velocity of 500 km/s and a typical  $d_i$  of 500 km based on  
 268 the density value  $n \sim 0.2$  cm $^{-3}$  (see Fig.2(b)-(c)). However, the number of intervals  
 269 does not change for  $\tau = 0.5$  s.

270 Figure 3 shows the distribution of the data points of the interval shown in Fig.2  
 271 in the parameter space  $\beta_{e,\parallel} - T_{e,\parallel}/T_{e,\perp}$ , together with the EFI thresholds corresponding  
 272 to growth rates  $\gamma/\Omega_{ce} = 0.001$  (dark red curve), 0.01 (orange curve), and 0.1 (yellow  
 273 curve) (see (Gary & Nishimura, 2003) for the values of the parameters used in the curves  
 274 for different  $\gamma$  values). Only a few data points exceed the  $\gamma/\Omega_{ce} = 0.001$  and 0.01 thresh-  
 275 old, while no points are found above  $\gamma/\Omega_{ce} = 0.1$ , suggesting that the EFI plays a key  
 276 role in shaping the electron distribution function.

277 From all the intervals where the threshold is exceeded, we select the ones composed  
 278 of at least two data points and for which  $\beta_{e,\parallel} < 30$ . We exclude intervals with large  
 279  $\beta_{e,\parallel}$  because, as it can be inferred from Fig.3, even small fluctuations of  $T_{e,\parallel}/T_{e,\perp}$  due  
 280 to instrumental noise can yield to  $\mathcal{T}_{\text{EFI}} > 0$  when  $\beta_{e,\parallel}$  is large, even though  $T_{e,\parallel}/T_{e,\perp} \sim$   
 281 1 so that the available free energy would not be enough for the instability to develop.  
 282 In addition, we select the intervals where magnetic field fluctuations could be identified  
 283 by visual inspection, allowing us to thoroughly perform the wave analysis. Using these

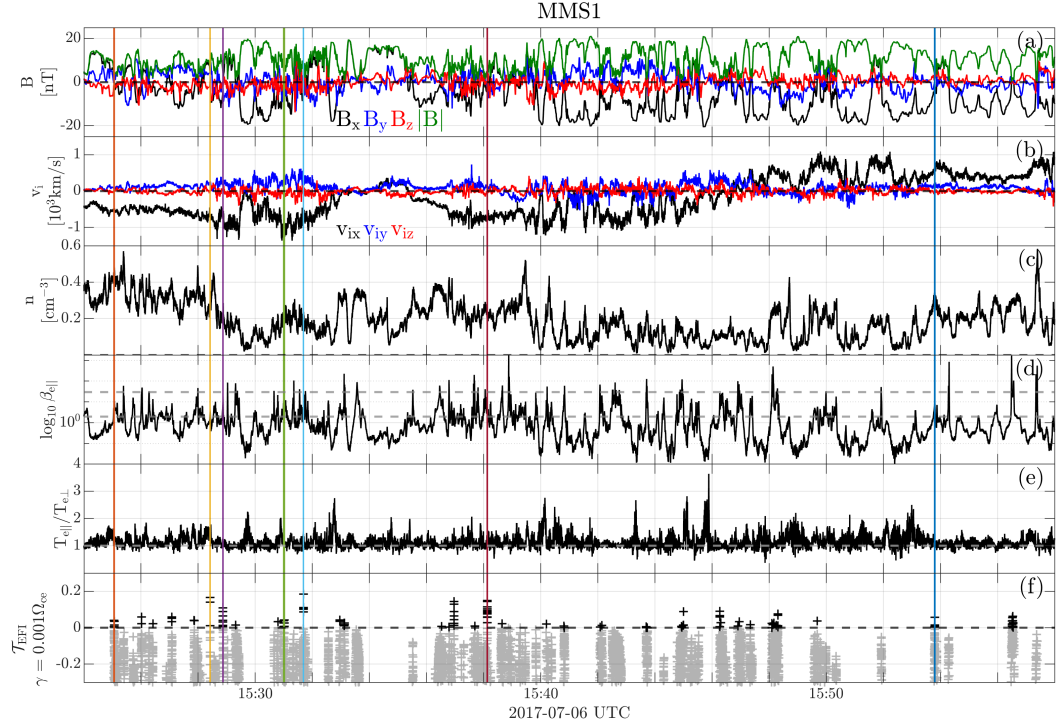


**Figure 2.** Overview of the current sheet flapping event in the Earth’s magnetotail. (a) Magnetic field; (b) Ion velocity; (c) Ion number density; (d)  $\log_{10} \beta_{e,\parallel}$ , the grey horizontal dashed lines correspond to  $\beta_{e,\parallel} = 2$  and  $\beta_{e,\parallel} = 30$ ; (e) Electron temperature anisotropy  $T_{e,\parallel}/T_{e,\perp}$ . (f) Electron firehose instability threshold  $\mathcal{T}_{\text{EFI}} = \frac{T_{e,\parallel}}{T_{e,\perp}} - (1 - S'_e/\beta_{e,\parallel}^{\alpha'_e})^{-1}$  for  $\gamma = 0.001\Omega_{ce}$ . Data points with  $\mathcal{T}_{\text{EFI}} > 0$  (black crosses) are unstable to the EFI. The vertical colored lines indicate the intervals with  $\mathcal{T}_{\text{EFI}} > 0$  that are selected based on the criteria discussed in Sec. 4 and that exhibit EF fluctuations.

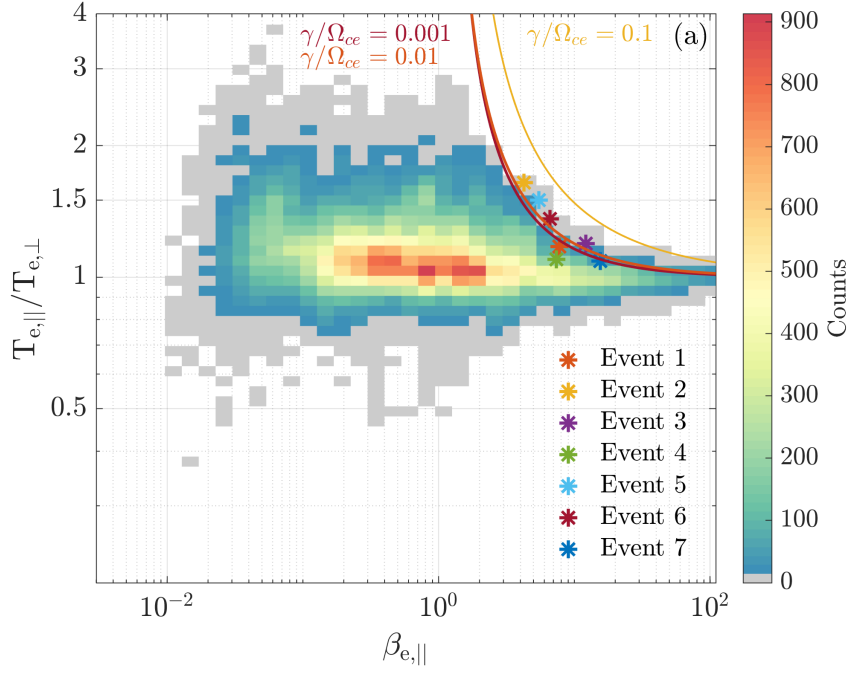


**Figure 3.** (a) Electron distribution in the parameter space  $\beta_{e,\parallel}-T_{e,\perp}/T_{e,\parallel}$ . The counts are scaled with bin size. The curves corresponds to the EFI threshold (see Eq. 1) for growth rates  $\gamma/\Omega_{ce}=0.001$  (dark red curve),  $0.01$  (orange curve), and  $0.1$  (yellow curve). The colored stars mark the average value of  $\beta_{e,\parallel}$  and  $T_{e,\parallel}/T_{e,\perp}$  during the intervals of the selected events identified with the correspondingly color-coded vertical lines in Fig.2.

**Table 1.** Time intervals and characteristics of the events selected for the EF wave analysis.  $\Delta t_{\mathcal{T}_{\text{EFI}} > 0}$  is the time interval where the EFI threshold is exceeded.

#	$\Delta t_{\mathcal{T}_{\text{EFI}} > 0}$ [UTC]	$\beta_{e,\parallel}$	$T_{e,\parallel}/T_{e,\perp}$	$T_{e,\parallel}$ [eV]	$T_{e,\perp}$ [eV]	$T_i$ [eV]	B  [nT]	$n$ [ $\text{cm}^{-3}$ ]
1	15:25:03.000–15:25:03.744	7.75	1.17	457	389	3259	3.3	0.47
2	15:28:25.070–15:28:25.134	4.24	1.64	1113	676	3840	5.8	0.32
3	15:28:52.010–15:28:52.284	12.17	1.19	1870	1567	4685	3.5	0.20
4	15:30:59.690–15:31:01.340	7.34	1.10	2678	2439	5178	5.5	0.20
5	15:31:41.150–15:31:41.300	5.46	1.50	2277	1516	5559	5.6	0.19
6	15:38:07.400–15:38:07.890	6.62	1.36	839	617	4844	3.3	0.22
7	15:53:47.700–15:53:48.430	15.48	1.12	668	596	4258	2.3	0.33

284 selection criteria, we retain seven intervals with  $\mathcal{T}_{\text{EFI}} > 0$ . They are marked with the  
 285 vertical lines in Fig.2. The coloured stars in Fig.3 mark  $\beta_{e,\parallel}$  and  $T_{e,\parallel}/T_{e,\perp}$  averaged dur-  
 286 ing the intervals identified with the correspondingly colour-coded vertical lines in Fig.2.  
 287 The time intervals of the seven selected events are summarized in Table 1, together with  
 288 the corresponding averaged plasma parameters.

289 In summary, we identify several intervals in which the EFI threshold is exceeded  
 290 while MMS is sampling the outflow reconnection region in the Earth’s magnetotail dur-  
 291 ing a current sheet flapping event. After applying the selection criteria discussed above,  
 292 we select seven events exhibiting wave activity at the time when the EFI threshold is ex-  
 293 ceeded. In the following, we will investigate the wave properties and establish whether  
 294 the observed fluctuations are compatible with EFI-originated waves.

## 295 5 Wave Analysis

296 In this Section, we present the detailed wave analysis of two of the seven selected  
 297 events (event #6 and #7), which we use to illustrate the typical wave properties. The  
 298 other events are discussed later in section 7. Event #6 exhibits very clear wave activ-  
 299 ity and a significant electron temperature anisotropy peaking at  $T_{e,\parallel}/T_{e,\perp} \sim 1.48$ . How-  
 300 ever, the analyzed waves are not co-located with the interval where the EFI threshold  
 301 is exceeded. So, we show also the detailed analysis of another event, event #7, during  
 302 which we identify two intervals of wave activity. One is co-located with the interval with  
 303  $\mathcal{T}_{\text{EFI}} > 0$  and the other, similarly to event #6, is observed immediately after the inter-  
 304 val where the EFI threshold is exceeded. Also, event #6 is characterized by  $V_{i,x} < 0$ ,  
 305 meaning that MMS is observing the tailward reconnection outflow, while event #7 is ob-  
 306 served in the Earthward outflow region. Hence, choosing these two events allows us to  
 307 show the properties of the observed waves both in Earthward and tailward outflow re-  
 308 gions. We aim to compare the observed wave characteristics to the theoretical expecta-  
 309 tions for EFI-generated fluctuations. As previously discussed, we focus on the non-propagating  
 310 EF mode (oblique, resonant mode) as it is predicted to have a lower instability thresh-  
 311 old and a larger growth rate with respect to the propagating (parallel, non-resonant) mode.

### 312 5.1 Event #6

313 An overview of event #6 is shown in Fig. 4. Figure 4(e) shows that during the in-  
 314 terval  $\Delta t_{\mathcal{T}_{\text{EFI}} > 0} = 15:38:07.400\text{--}15:38:07.890$ , highlighted with the red-shaded area, the

315 temperature anisotropy  $T_{e,\parallel}/T_{e,\perp}$  exceeds the EFI threshold (red line, see Eq. 1) and  
 316 it reaches a maximum value of 1.5. In addition,  $\beta_{e,\parallel}$  has moderate values ( $\beta_{e,\parallel} \sim 7$  is  
 317 the average  $\beta_{e,\parallel}$  in the interval where the instability threshold is reached, see Fig.4(d)).  
 318 The magnetic field is shown in Fig.4(a) and the relatively low magnitude of  $|B| \sim 6$  nT  
 319 suggests that MMS is sampling the plasma sheet. MMS also observed a strong electron  
 320 (and ion, not shown) flow mainly directed along the x GSM direction with  $|v_{e,x}| \sim 1500$  km/s  
 321 suggesting that MMS is sampling the reconnection outflow region (see Fig.4(c)).

322 Figures 4(f) and (g) show the wavelet spectrograms of the electric and magnetic  
 323 field power. Both electric and magnetic field power increase in the yellow-shaded inter-  
 324 val. The fluctuations are rather broadband but they exhibit a peak at a few Hz, close  
 325 to the lower hybrid frequency  $f_{LH} = \sqrt{f_{ci}f_{ce}}$  ( $f_{ci}$  and  $f_{ce}$  are respectively the ion and elec-  
 326 tron cyclotron frequency). As a first step, we isolate the high-frequency fluctuations from  
 327 the lower-frequency variations of the magnetic field. We define the filtering frequency  
 328  $f_{filt}$  by requiring that the magnetic field signal filtered in the frequency range  $f < f_{filt}$   
 329 exhibits all the main magnetic structures of the unfiltered signal. In this case we choose  
 330  $f_{filt} = 2.6$  Hz (see Fig.4(a)). The magnetic field exhibits low frequency variations ( $f <$   
 331  $f_{filt}$ , Fig.4(a)) and, interestingly, higher frequency fluctuations ( $f > f_{filt}$  showing wave  
 332 activity Fig.4(b)). The interval with enhanced wave activity  $\Delta t = 15:38:08.0 - 15:38:11.0$   
 333 is highlighted by the yellow-shaded area. The magnetic field fluctuations  $\delta B$  have sim-  
 334 ilar amplitude in all three components, both in the GSM coordinate system (see Fig.5(b))  
 335 and in field-aligned coordinates (see Fig.4(b)).

336 To better characterize the observed waves, we compute the dispersion relation from  
 337 the phase differences of  $\delta B_z$  between spacecraft pairs, applying the multi-spacecraft in-  
 338 terferometry method (Graham et al., 2016, 2019) to the time interval  $\Delta t$ . Figure 4(h)  
 339 shows that the normalized power  $P(f, k)/P_{max}$  increases in the frequency range  $2.6$  Hz  $<$   
 340  $f < 3.8$  Hz (black dashed lines) with a peak at  $f = f_{obs} = 3.2$  Hz (black star). The  
 341 wave number at the  $P(f, k)/P_{max}$  peak is  $k\rho_e \sim 0.4$  ( $\rho_e \sim 26$  km is the electron gyro-  
 342 radius averaged over  $\Delta t$ ) which corresponds to the wave phase speed in the spacecraft  
 343 reference frame of  $v_{ph} \sim 900$  km/s. Figures 4(i) and (j) show that the wave vector  $\mathbf{k}$   
 344 is directed mainly along the x direction, i.e. aligned with the direction of the plasma flow.  
 345 The average wave vector direction is  $\hat{\mathbf{k}} = [-0.82, 0.43, -0.38]$  GSM.

346 In addition, we estimate the uncertainty of the wave vector  $\Delta k\rho_e$ . Even though the  
 347  $P(k_x, k_z)/P_{max}$  and  $P(k_y, k_z)/P_{max}$  distributions exhibit a clear peak (Fig.4(i)–(j)), they  
 348 are characterized by a certain spread in the  $(k_x, k_z)$  and  $(k_y, k_z)$  parameter space respec-  
 349 tively. To compute the observed wave vector uncertainty  $\Delta k\rho_e$ , we consider all the points  
 350 for which the power  $P(k_i, k_j)$  is above 10% of the maximum power  $P_{max}$  in Fig.4(i)–(j),  
 351 where  $i, j = x, y, z$ . The area selected with this criterion is shown in brighter colors in  
 352 Fig.4(i)–(j). For each wave vector component  $k_j$ , the minimum  $k_j$  for which the power  
 353  $P(k_i, k_j)$  is larger than 10% of the maximum power  $P_{max}$  is  $k_{j,min}(P = 0.1P_{max})$ . Anal-  
 354 ogously,  $k_{j,max}(P = 0.1P_{max})$  is the maximum value of  $k_j$  for which the power  $P(k_i, k_j)$   
 355 is equal or larger than 10% of the maximum power  $P_{max}$ . In general,  $k_{j,min}(P = 0.1P_{max})$   
 356 and  $k_{j,max}(P = 0.1P_{max})$  are asymmetric with respect to  $k_j$  corresponding to the max-  
 357 imum power. A simple way to symmetrize the uncertainty with respect to  $k_j$  is to use  
 358 the average between the two uncertainties  $k_{j,min}(P = 0.1P_{max})$  and  $k_{j,max}(P = 0.1P_{max})$   
 359 so that the uncertainty  $\Delta k_j\rho_e$  of the wave vector  $j^{\text{th}}$  component is  $\Delta k_j\rho_e = \frac{\rho_e}{2}[k_{j,max}(P =$   
 360  $0.1P_{max}) - k_{j,min}(P = 0.1P_{max})]$ . We then compute the uncertainty of the wave vec-  
 361 tor magnitude  $\Delta k\rho_e$ . We obtain  $\Delta k\rho_e \sim 0.17 \sim 0.41k\rho_e$  which is quite significant but  
 362 expected, taking into account the considerable variability of the observed quantities.

363 Figure 5 shows additional characteristics of the observed fluctuations that are cru-  
 364 cial to establishing whether the observed waves are indeed associated with the EFI. As  
 365 discussed in Section 2, the non-propagating EF mode is characterized by zero real fre-  
 366 quency  $f = \omega/2\pi = 0$ ,  $k\rho_e \lesssim 1$ , the wave vector is directed obliquely with respect to  
 367 the background magnetic field, and it is an electromagnetic mode. In addition, theoret-

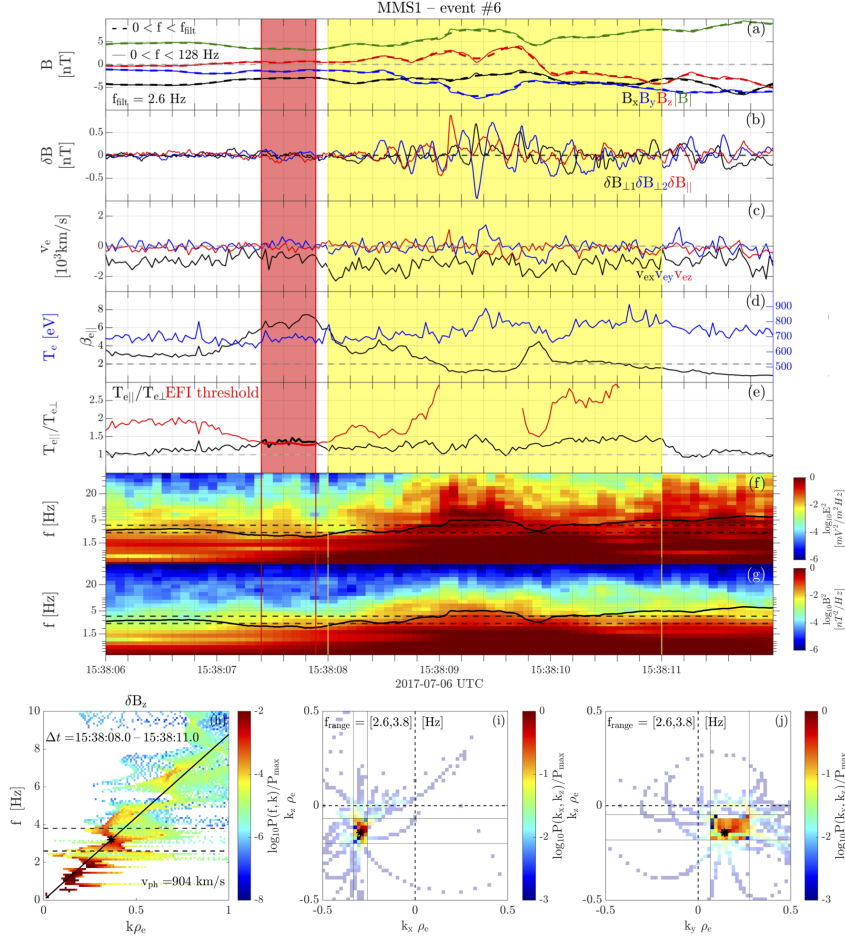


**Figure 4.** Top: (a) Magnetic field components and magnitude. The solid lines are the unfiltered magnetic field, with frequencies in the FGM frequency range  $[0, 128]$  Hz, the dashed thick lines are the filtered signal with frequencies in the range  $[0, f_{\text{filt}}]$  where  $f_{\text{filt}} = 2.6$  Hz. (b) Magnetic field fluctuations ( $f > 2.6$  Hz) in field-aligned coordinates (FAC). (c) Electron velocity. (d)  $\beta_{e,\parallel}$  and electron temperature  $T_e$ . (e) Electron temperature anisotropy  $T_{e,\parallel}/T_{e,\perp}$  and the EFI threshold based on Eq. 1. (f) Magnetic field wave power. (g) Electric field wave power. The black line is the lower hybrid frequency  $f_{\text{LH}}$  and the dashed black lines corresponding to  $f = 2.6$  Hz and  $f = 3.8$  Hz indicate the frequency range of the observed fluctuations. Bottom: Normalized power of magnetic field fluctuations  $\delta B_z$  versus (h)  $k\rho_e$  and frequency  $f$ ; (i)  $k_x\rho_e$  and  $k_z\rho_e$  (in the frequency range  $\Delta f = [2.6, 3.8]$  Hz); (j)  $k_y\rho_e$  and  $k_z\rho_e$  (in the frequency range  $\Delta f = [2.6, 3.8]$  Hz). The dashed lines in panel (h) correspond to  $f = 2.6$  Hz and  $f = 3.8$  Hz. The area with brighter color in panel (i) and (j) contains all the points with power  $P(k_x, k_z)$  (and  $P(k_y, k_z)$ ) larger than 10% of the maximum power  $P_{\text{max}}$ , i.e.  $P(k_x, k_z) > 0.1P_{\text{max}}$  and  $P(k_y, k_z) > 0.1P_{\text{max}}$ .

368 ical expectations about the non-propagating EF mode include  $\zeta_e^\pm \lesssim 1$ , i.e. the mode  
 369 is resonant with electrons.

370 Figure 5 shows that the characteristics of the observed fluctuations are compat-  
 371 ible with the theoretical predictions listed above. Firstly, we establish that the observed  
 372 mode is non-propagating in the plasma reference frame, i.e. the Doppler-shifted frequency  
 373 is zero ( $f_{\text{obs}} - f_{\text{DS}} = f_{\text{obs}} - (\mathbf{v}_e \cdot \mathbf{k})/2\pi = 0$ , where  $f_{\text{DS}} = (\mathbf{v}_e \cdot \mathbf{k})/2\pi$  is the Doppler shift  
 374 frequency) or, equivalently,  $f_{\text{obs}} = f_{\text{DS}}$ . To do that, we compare the observed frequency  
 375 of the fluctuations ( $f_{\text{obs}}$ , red solid thick line in Fig.5(c)) to the Doppler shift frequency  
 376  $f_{\text{DS}}$  (black solid thick line in Fig.5(c)) in the time interval  $\Delta t$  where the waves are ob-  
 377 served (yellow shaded interval in Fig.4). The Doppler shift frequency  $f_{\text{DS}}$  is significant  
 378 as the wave vector  $\mathbf{k}$  is quite aligned with the electron velocity  $\mathbf{v}_e$ . In particular, Fig.5(d)  
 379 shows that  $\theta_{\mathbf{k}\mathbf{v}_e} < 60^\circ$  during the considered time interval and the average  $\langle \theta_{\mathbf{k}\mathbf{v}_e} \rangle_{\Delta t} \sim$   
 380  $38^\circ$ , where  $\theta_{\mathbf{k}\mathbf{v}_e}$  is the angle between  $\mathbf{k}$  and  $\mathbf{v}_e$ . The time series of the Doppler shift fre-  
 381 quency  $f_{\text{DS}}$  displays significant variations, which are due to the variations of the electron  
 382 velocity  $\mathbf{v}_e$ . To account for the variability of  $f_{\text{DS}}$ , we compute  $\sigma_{f_{\text{DS}}}$  which includes the  
 383 wave vector uncertainty  $\Delta k_{\rho_e}$  and the standard deviation of  $\mathbf{v}_e$  computed across the in-  
 384 terval  $\Delta t$ . The quantity  $\sigma_{f_{\text{DS}}}$  corresponds to the uncertainty of  $f_{\text{DS}}$ . The grey area in Fig.5(c)  
 385 contains the points with  $f_{\text{DS}} - \sigma_{f_{\text{DS}}} < f < f_{\text{DS}} + \sigma_{f_{\text{DS}}}$  and defines the range of variabil-  
 386 ity of  $f_{\text{DS}}$ . Fig.5(c) also shows the time-averaged values across the interval ( $\langle f_{\text{DS}} \rangle_{\Delta t} -$   
 387  $\sigma_{f_{\text{DS}}}$ ,  $\langle f_{\text{DS}} \rangle_{\Delta t}$ ,  $\langle f_{\text{DS}} \rangle_{\Delta t} + \sigma_{f_{\text{DS}}}$ ) as black dashed lines. The observed frequency  $f_{\text{obs}}$  lies be-  
 388 tween  $\langle f_{\text{DS}} \rangle_{\Delta t} - \sigma_{f_{\text{DS}}}$  and  $\langle f_{\text{DS}} \rangle_{\Delta t} + \sigma_{f_{\text{DS}}}$  and for the majority of the time points  $f_{\text{obs}}$   
 389 lies in the variability range of  $f_{\text{DS}}$ . We conclude that the observed Doppler-shifted fre-  
 390 quency is close to zero and the observed waves are hence non-propagating fluctuations.

391 Figure 5(d) shows that the wave vector is oblique with respect to the background  
 392 magnetic field. Fig.5(e) shows the spectrogram of  $\mathcal{E}_{\text{long}}$  which, while displaying signif-  
 393 icant variability, assumes relatively low values for the majority of the interval. The value  
 394 of  $\mathcal{E}_{\text{long}}$  averaged both in time across  $\Delta t$  and in the frequency range  $\Delta f = [2.6, 3.8]$  Hz  
 395 is  $\langle \mathcal{E}_{\text{long}} \rangle_{\Delta t, \Delta f} \sim 0.54$ . This means that the fluctuations are not electrostatic and they  
 396 have a significant electromagnetic component. Also,  $\langle \zeta_e^\pm \rangle_{\Delta t} \sim 1.7$  (not shown), indi-  
 397 cating that electrons have a relatively strong resonance.

398 Hence, we observe non-propagating fluctuations characterized by a wave vector  $k_{\rho_e} \sim$   
 399  $0.4$  directed obliquely with respect to the background magnetic field, with significant elec-  
 400 tromagnetic component, and resonant electrons. All these characteristics are consistent  
 401 with the theoretical expectations for EFI-generated fluctuations.

## 402 5.2 Event #7

403 As shown in Fig.4, during event #6 the interval where the EFI threshold is exceeded  
 404 ( $\Delta t_{\mathcal{T}_{\text{EFI}} > 0} = 15:38:07.400\text{--}15:38:07.890$ ) and the interval exhibiting the strong wave ac-  
 405 tivity ( $\Delta t = 15:38:08.000\text{--}15:38:11.000$ ) are not co-located, albeit the waves are observed  
 406 immediately after the region with  $\mathcal{T}_{\text{EFI}} > 0$ . In this Section, we present the detailed  
 407 analysis of event #7 which exhibits wave activity both co-located with and, like event  
 408 #6, immediately after the interval with  $\mathcal{T}_{\text{EFI}} > 0$ . The observed fluctuations during event  
 409 #7 are very similar to the ones reported in event #6 and are also consistent with EFI-  
 410 generated waves.

411 Figure 6 is analogous to Fig.4 for event #6 and it shows that during event #7 the  
 412 EFI threshold is exceeded in interval  $\Delta t_{\mathcal{T}_{\text{EFI}} > 0} = 15:53:47.700\text{--}15:53:48.430$  between the  
 413 vertical red lines (see in particular Fig. 6(e)), where  $\beta_{e,\parallel}$  increases to a maximum value  
 414 of 28 (Fig. 6(d)) as MMS is located close to the neutral line. The magnetic field mag-  
 415 nitude is  $|\mathbf{B}| \sim 2$  nT (Fig. 6(a)) and MMS observes a strong electron flow, mainly along  
 416 the outflow in the GSM x direction reaching  $|v_{e,x}| \sim 1200$  km/s (Fig.6(c)). Figure 6(b)  
 417 shows the magnetic field fluctuations  $\delta \mathbf{B}$  ( $f_{\text{filt}} = 2.5$  Hz) which have similar amplitude  
 418 in all three components in both intervals of wave activity. Both magnetic and electric

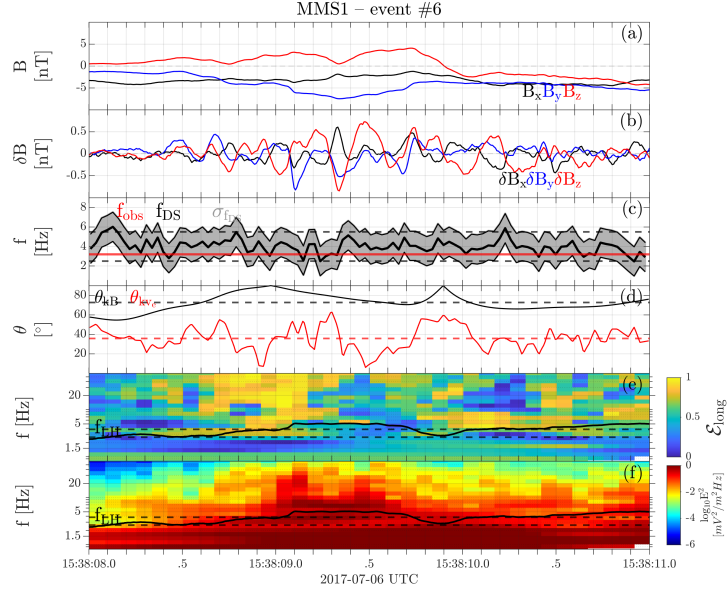


**Figure 5.** (a) Magnetic field; (b) Magnetic field fluctuations; (c) Observed frequency  $f_{\text{obs}}$  (red solid line), Doppler-shift frequency  $f_{\text{DS}}$  (solid black line) and associated variability range (grey shaded region) with value  $\sigma_{f_{\text{DS}}}$ . The central dashed black lines correspond to the time-averaged Doppler shift frequency  $\langle f_{\text{DS}} \rangle$ , the top and bottom dashed lines are  $\langle f_{\text{DS}} \rangle + \sigma_{f_{\text{DS}}}$  and  $\langle f_{\text{DS}} \rangle - \sigma_{f_{\text{DS}}}$ . (d) Angle between the wave vector direction and background magnetic field direction  $\theta_{\text{kB}}$  and angle between the wave vector direction and electron velocity direction  $\theta_{\text{kve}}$ . (e) Spectrogram of  $\mathcal{E}_{\text{long}}$ . (f) Spectrogram of the electric field power. The black line is the lower hybrid frequency  $f_{\text{LH}}$  and the dashed black lines indicate the frequency range of the observed fluctuations ( $\Delta f = [2.6, 3.8]$  Hz). The time interval shown in this figure corresponds to the yellow-shaded interval in Fig.4.

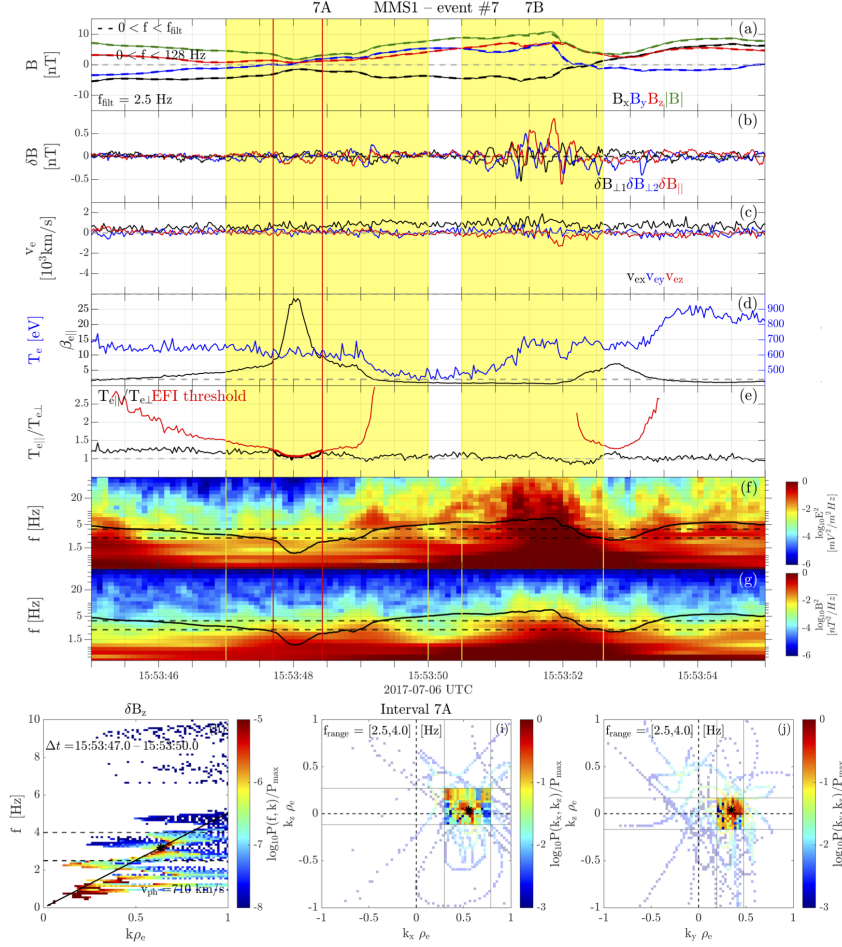


**Figure 6.** Same as Fig.4 for event #7. In this case,  $f_{\text{filt}} = 2.5$  Hz. The bottom panels show the results of the multi-spacecraft interferometry method applied to interval 7A and The dashed lines in panel (h) correspond to  $f = 2.5$  Hz and  $f = 4.0$  Hz.

419 field power increase in the intervals with wave activity (Fig.6(f) and (g)). As mentioned  
 420 above, we identify two intervals characterized by wave activity: interval 7A ( $\Delta t_A = 15:53:47.0$ –  
 421  $15:53:50.0$ ), which encloses the interval with  $\mathcal{T}_{\text{EFI}} > 0$  and interval 7B ( $\Delta t_B = 15:53:50.5$ –  
 422  $15:53:53.0$ ). The fluctuations have larger amplitude in interval 7B, which is not co-located  
 423 with the interval where the instability threshold is exceeded. In the following, we will  
 424 focus in particular on the analysis of the fluctuations observed in interval  $\Delta t_A$ .

425 We use the multi-spacecraft interferometry method (Graham et al., 2016, 2019) to  
 426 establish the characteristics of the fluctuations in  $\Delta t_A$ . The normalized power of the mag-  
 427 netic field fluctuations  $P(f, \mathbf{k})/P_{\text{max}}$  increases in the frequency range  $\Delta f = [2.5, 4.0]$  Hz  
 428 (black dashed lines in Fig.6(h)) and peaks at  $f = f_{\text{obs}} = 3.2$  Hz (black star). The wave  
 429 number at the peak of  $\delta B_z$  normalized power  $P(f, \mathbf{k})/P_{\text{max}}$  is  $k\rho_e \sim 0.66$  ( $\rho_e \sim 22$  km  
 430 is the electron gyroradius averaged over interval 7A) which corresponds to phase speed  
 431 in the spacecraft reference frame of  $v_{\text{ph}} \sim 710$  km/s. Figure 6(i) and (j) shows that the  
 432 wave vector  $\mathbf{k}$  is directed mainly along x GSM and aligned with the direction of the out-  
 433 flow ( $\hat{\mathbf{k}} = [0.78, 0.61, 0.03]$  GSM). Analogously to event #6, we estimate the uncer-  
 434 tainty of the wave vector magnitude  $\Delta k\rho_e$  and we obtain  $\Delta k\rho_e \sim 0.22 \sim 0.33 k\rho_e$ .

435 Similarly as Fig.5 for event #6, Figure 7 shows the property of the fluctuations in  
 436 interval 7A to establish whether the observations are consistent with theoretical expect-  
 437 ations for the EF fluctuations. Fig.7(a) indicates that the waves observed in  $\Delta t_A$  can  
 438 be considered as non propagating, as  $f_{\text{obs}}$  lies between  $\langle f_{\text{DS}} \rangle_{\Delta t} - \sigma_{f_{\text{DS}}}$  and  $\langle f_{\text{DS}} \rangle_{\Delta t} + \sigma_{f_{\text{DS}}}$   
 439 and for the majority of the time points  $f_{\text{obs}}$  lies in the variability range (gray area of Fig.7(a))  
 440 of  $f_{\text{DS}}$ . Also in this case, the contribution of  $f_{\text{DS}}$  to the Doppler shifted frequency is sig-  
 441 nificant as  $\langle \theta_{k_{\text{ve}}} \rangle_{\Delta t} \sim 36^\circ$  in interval 7A (see Fig.7(d)).

442 Other characteristics of the fluctuations in interval 7A include  $\langle \mathcal{E}_{\text{long}} \rangle_{\Delta t, \Delta f} \sim 0.23$ ,  
 443 indicating that they are electromagnetic (in this case  $\Delta f = [2.5, 4.0]$  Hz). The spectro-  
 444 gram of  $\mathcal{E}_{\text{long}}$  is shown in Fig.7(e) and despite exhibiting some variability, it never reaches  
 445 values close to 1 in the considered  $\Delta f$  during interval 7A. Also, electrons are resonant  
 446 since  $\langle \zeta_e^\pm \rangle_{\Delta t} \sim 1.2$  (not shown). The angle between the wave vector and the background  
 447 magnetic field  $\theta_{\text{kB}}$  changes significantly in interval 7A, going from a minimum value of  
 448  $\theta_{\text{kB}} \sim 30^\circ$  to values close to  $90^\circ$  (Fig.7(d)), while the time-averaged value of the wave  
 449 normal angle is  $\langle \theta_{\text{kB}} \rangle_{\Delta t} \sim 69^\circ$ . The strong variation of  $\theta_{\text{kB}}$  across  $\Delta t_A$  is due to the  
 450 changing background magnetic field direction. In particular  $B_y$  goes from negative  $B_y \sim$   
 451  $-1$  nT to positive  $B_y \sim 5$  nT in the considered interval. However, for the majority of  
 452 the interval  $\theta_{\text{kB}} > 30^\circ$ , so that the wave vector can be considered to be oblique with  
 453 respect to the background magnetic field.

454 In summary, we observe non-propagating fluctuations with wave vector  $k\rho_e \sim 0.66$   
 455 directed obliquely with respect to the background magnetic field. The fluctuations have  
 456 a significant electromagnetic component and are resonant with electrons. We conclude  
 457 that the observed fluctuations are generated by the EFI instability as they exhibit the  
 458 characteristics associated with the non-propagating EF mode. As mentioned above, event  
 459 #7 presents two intervals with wave activity. We have shown the detailed wave analy-  
 460 sis of the fluctuations in interval 7A, which are co-located with the region where the EFI  
 461 threshold is exceeded. The fluctuations with larger amplitude observed in interval 7B  
 462 have similar characteristics (not shown) and we conclude that they are also EFI-generated  
 463 waves. It is reasonable to expect that the development of the waves and the increase in  
 464 the wave amplitude results in a decrease in the temperature anisotropy, which is reduced  
 465 to a value close to isotropic.

## 466 6 Comparison between In Situ Observations and Model

467 To corroborate our conclusion that the observed fluctuations are EFI-generated,  
 468 we compare the MMS observations with the results of the numerical solver PDRK (Xie  
 469 & Xiao, 2016), which has been used to obtain Fig.1. The model implemented in the solver  
 470 assumes that the plasma is homogeneous, as well as the background magnetic field. We  
 471 consider a quasi-neutral plasma composed of electrons and protons. In the following, we  
 472 will refer to the protons as ions, for consistency with MMS notation. We use a non-drifting  
 473 bi-Maxwellian distribution function with  $T_{e,\parallel}/T_{e,\perp} > 1$  for electrons and a non-drifting  
 474 Maxwellian distribution function for ions as input. The ion temperature is assumed to  
 475 be isotropic  $T_i = T_{i,\parallel} = T_{i,\perp}$ . This approximation is motivated by the fact that the  
 476 non-propagating EF mode is not affected by the ion temperature anisotropy (López et  
 477 al., 2022; Maneva et al., 2016). The PDRK solver input parameters are obtained by av-  
 478 eraging the relevant observed quantities in the interval  $\Delta t_{\tau_{\text{EFI}} > 0}$ , where the EFI thresh-  
 479 old is exceeded. The input parameters for the seven observed events are collected in Ta-  
 480 ble 1. To avoid confusion, in this section the quantities that resulted from the analysis  
 481 of in situ spacecraft observations are labeled with the subscript [obs].

482 Figure 8 shows the results of the PDRK solver with input parameters mimicking  
 483 the in situ observations of event #6. A positive growth rate  $\gamma$  is obtained for several points  
 484 in the parameter space  $k\rho_e - \theta_{\text{kB}}$  with the maximum growth rate  $\gamma_{\text{max}}/\Omega_{ce} \sim 0.025$  at  
 485  $[k\rho_e, \theta_{\text{kB}}] = [0.54, 58^\circ]$  (see Fig.8(a)). The unstable wave mode is characterized by zero

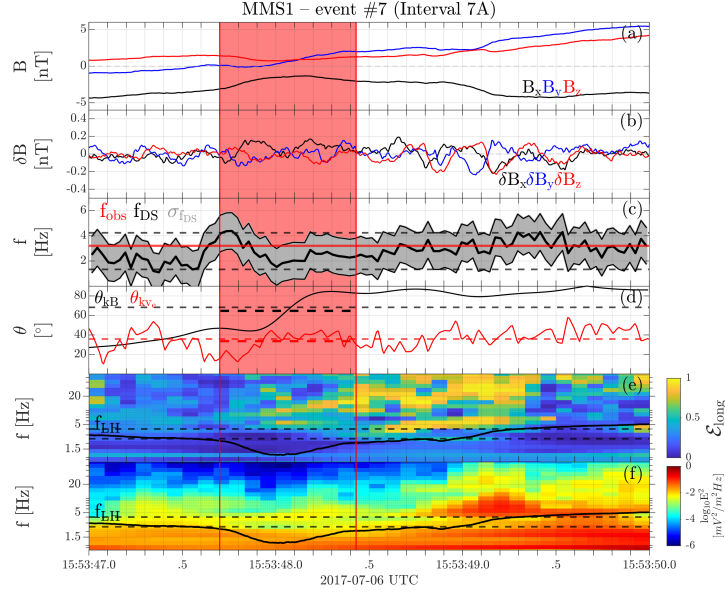


**Figure 7.** Same as Fig.5 for event #7 (interval 7A). In this case, the interval with  $\mathcal{T}_{\text{EFI}} > 0$  (red-shaded region) is co-located with the wave activity. Panel (c) shows  $\theta_{\text{kB}}$  and  $\theta_{\text{kve}}$ . The dashed lines correspond to the average value of  $\theta_{\text{kB}}$  and  $\theta_{\text{kve}}$  and they extend over the time interval where they are computed.

486 real frequency (see Fig.8(b)). The values of  $\theta_{\text{kB}}$  associated with highest wave growth range  
 487 between  $52^\circ$  and  $64^\circ$  and indicate that the mode is oblique (see Fig.8(a)). The values  
 488 of  $\mathcal{E}_{\text{long}}$ , which are below 0.8 for the majority of the points in the area of the param-  
 489 eter space with positive growth rate, indicate that the mode is electromagnetic (see Fig.8(d)).  
 490 We conclude that the unstable mode is the non-propagating EF mode, as expected con-  
 491 sidering the imposed input electron distribution function with  $T_{e,\parallel}/T_{e,\perp} > 1$ .

492 Figure 8 shows that the results of the numerical solver are consistent with in situ  
 493 observations, providing further evidence that the observed fluctuations are associated  
 494 with the EFI. The observed  $[\theta_{\text{kB}}]_{\text{obs}} \sim 61^\circ$  and  $[k\rho_e]_{\text{obs}} \sim 0.41$ , corresponding to max-  
 495 imum magnetic field fluctuations normalized power  $P(k, f)/P_{\text{max}}$  in Fig.5(h), are marked  
 496 with red stars in Fig.8. The red-shaded area corresponds to the points in the param-  
 497 eters space which lay within  $[\Delta k\rho_e]_{\text{obs}}$  and  $[\Delta \theta_{\text{kB}}]_{\text{obs}}$ , the uncertainties of  $[k\rho_e]_{\text{obs}}$  and  $[\theta_{\text{kB}}]_{\text{obs}}$ .  
 498 The estimation of the wave vector uncertainty  $[\Delta k\rho_e]_{\text{obs}}$  is detailed in Sec.5. The uncer-  
 499 tainty of the wave-normal angle  $[\theta_{\text{kB}}]_{\text{obs}}$ ,  $[\Delta \theta_{\text{kB}}]_{\text{obs}}$ , is computed by considering  $[\Delta k_j \rho_e]_{\text{obs}}$   
 500 and the background magnetic field direction averaged in the interval  $\Delta t_{\mathcal{T}_{\text{EFI}} > 0}$ . As ex-  
 501 pected considering the significant variability of the observed quantities, the uncer-  
 502 tainties are significant,  $[\Delta k\rho_e]_{\text{obs}} \sim 0.17 \sim 0.41 [k\rho_e]_{\text{obs}}$  and  $[\Delta \theta_{\text{kB}}]_{\text{obs}} \sim 10^\circ \sim 0.16 [\theta_{\text{kB}}]_{\text{obs}}$ .  
 503 Nonetheless, Fig.8 shows a good agreement between the numerical results and the in situ  
 504 observations, as the observational points composing the red-shaded area significantly over-  
 505 lap with the EFI unstable region predicted by the numerical solver. The comparison be-  
 506 tween the output of the numerical solver and in situ MMS observations further confirms  
 507 the fact that the observed waves are EF fluctuations.

508 Analogously to Fig.8 for event #6, Figure 9 shows a good agreement between the  
 509 in situ observations and the numerical solver results for interval 7A of event #7. Fig-  
 510 ure 9(a) shows that a positive growth rate  $\gamma$  is obtained for several points in the param-  
 511 eter space  $k\rho_e - \theta_{\text{kB}}$ . The growth rate peaks ( $\gamma_{\text{max}}/\Omega_{\text{ce}} \sim 0.01$ ) at  $[k\rho_e, \theta_{\text{kB}}] = [0.56, 56^\circ]$

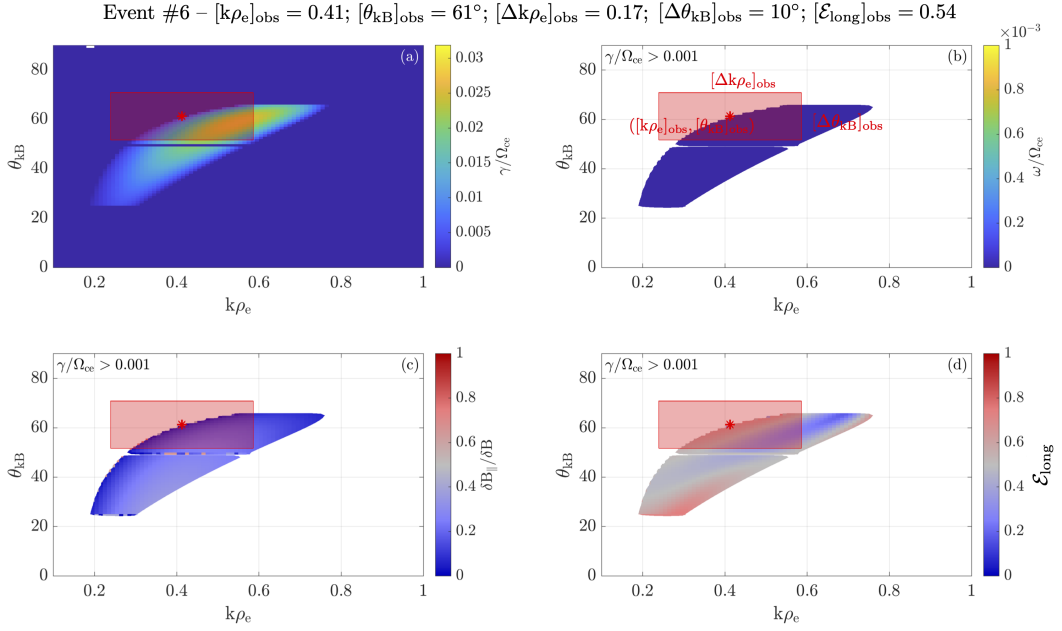


**Figure 8.** Observation–PDRK numerical solver comparison for event #6. The input parameters used in the numerical solver are  $T_{e,\parallel} = 839$  eV,  $T_{e,\perp} = 617$  eV, the background magnetic field  $B = 3.3$  nT and density  $n_e = n_i = n = 0.22$  cm $^{-3}$  while the isotropic ion temperature is  $T_i = T_{i,\parallel} = T_{i,\perp} = 4844$  eV (see Table 1). These values correspond to the average over the interval where the EFI threshold is exceeded ( $\Delta t_{\tau_{\text{EFI}} > 0} = 15:38:07.400$ – $15:38:07.890$ ).  $k\rho_e$  and  $\theta_{\text{kB}}$  versus (a) imaginary frequency  $\gamma/\Omega_{ce}$  (b) real frequency  $\omega/\Omega_{ce}$  (c)  $\delta B_{\parallel}/\delta B$  (d)  $\mathcal{E}_{\text{long}}$ . The quantities in panels (b)–(d) are shown for values of the growth rate exceeding the marginal stability condition, which is usually set at  $10^{-3}$  (Camporeale & Burgess, 2008). The values listed above panel (a) and (b) correspond to the values observed in situ. In each subplot, the red star corresponds to the observed  $k\rho_e$  and  $\theta_{\text{kB}}$  at the peak of normalized power of the fluctuations (see Fig.4(h)–(j)). The red-shaded area represents the uncertainty of these measurements,  $\Delta k\rho_e$  and  $\Delta\theta_{\text{kB}}$ .

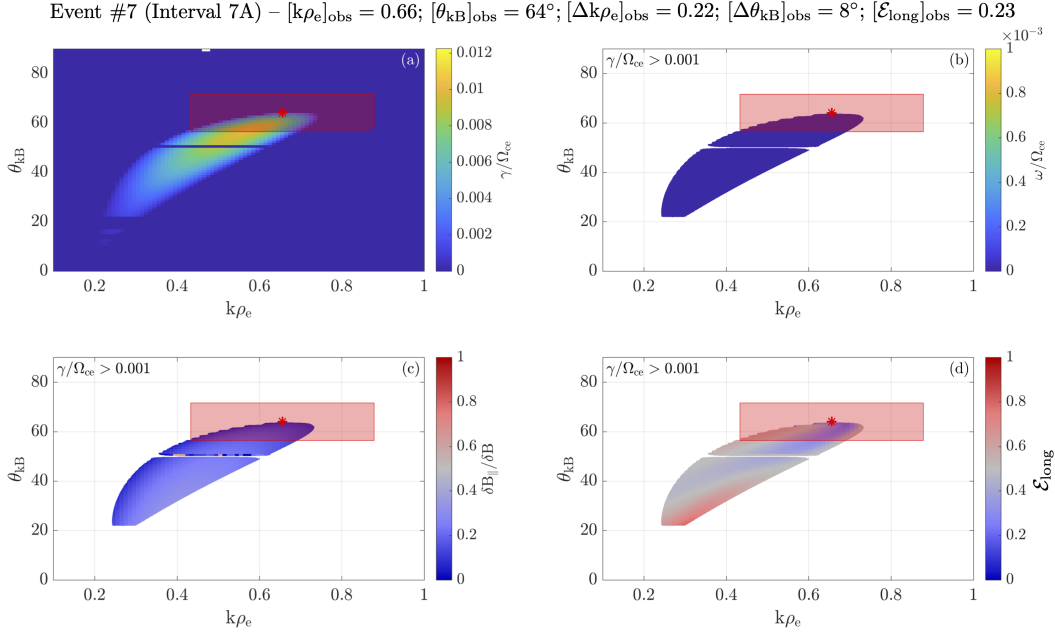


**Figure 9.** Observation–PDRK numerical solver comparison for event #7, analogous to Fig.8 for event #6. We use  $T_{e,\parallel} = 668$  eV,  $T_{e,\perp} = 596$  eV,  $B = 2.3$  nT,  $n_e = n_i = n = 0.33$  cm $^{-3}$  and  $T_i = T_{i,\parallel} = T_{i,\perp} = 4258$  eV, corresponding to the average over the interval where the EFI threshold is exceeded ( $\Delta t_{\mathcal{T}_{\text{EFI}} > 0} = 15:53:47.700\text{--}15:53:48.430$ ) as input parameters for the PRDK solver (see Table 1).

512 so the growing mode is rather oblique with respect to the background magnetic field. Fig.9(b)  
 513 shows that all the points associated with  $\gamma > 0$  have zero real frequency, so the mode  
 514 is non-propagating. Also,  $\mathcal{E}_{\text{long}} \lesssim 0.5$  for the majority of the points in the area of the  
 515 parameter space with  $\gamma > 0$ , suggesting that the mode is electromagnetic (Fig.9(d)).  
 516 Similar to what we concluded for event #6, these characteristics suggest that the un-  
 517 stable mode presented in Fig.9 is the non-propagating EF mode.

518 The wave analysis results of the observed fluctuations in interval 7A of event #7  
 519 are shown in Fig.9. In this case, the wave analysis of in situ observations gives  $[k\rho_e]_{\text{obs}} \sim$   
 520  $0.66$  and  $[\theta_{\text{kB}}]_{\text{obs}} \sim 64^\circ$  and the associated uncertainties  $[\Delta k\rho_e]_{\text{obs}} \sim 0.22 \sim 0.33$   $[k\rho_e]_{\text{obs}}$   
 521 and  $[\Delta\theta_{\text{kB}}]_{\text{obs}} \sim 8^\circ \sim 0.13$   $[\theta_{\text{kB}}]_{\text{obs}}$ . During event #7 (interval 7A), as well as for event  
 522 #6, we observe a good agreement between the in situ observations and the results of the  
 523 numerical solver, reinforcing the conclusion that the observed fluctuations are indeed con-  
 524 sistent with the non-propagating EF mode.

## 525 7 Other Events

526 As discussed in Section 4, during the interval shown in Fig.2 we have identified seven  
 527 intervals fulfilling  $\mathcal{T}_{\text{EFI}} > 0$  together with the selection criteria involving the number  
 528 of consecutive data points with  $\mathcal{T}_{\text{EFI}} > 0$ , the value of  $\beta_{e,\parallel}$  and the presence of wave  
 529 activity. For each of the events, we perform the detailed wave analysis presented in Sec. 5  
 530 and we compare the in situ observations with the numerical solver results, using the in-  
 531 put parameters reported in Table 1. Each event is defined by the interval where the EFI  
 532 threshold is exceeded ( $\Delta t_{\mathcal{T}_{\text{EFI}} > 0}$ , see Table 1) and by the interval where the wave activ-  
 533 ity is observed ( $\Delta t$ , see Table 2). As already discussed in Sec.5, event #7 presents two  
 534 intervals (7A and 7B) with enhanced wave activity.

535 For all the selected events, the observed fluctuations have characteristics consis-  
 536 tent with the non-propagating EF mode. The results of the analysis of the seven events  
 537 are summarized in Fig.10 and Table 2. In Figure 10, the abscissa shows the event num-  
 538 ber #. Fig.10(a) shows the observed frequency  $f_{\text{obs}}$  (black star) and the Doppler shift  
 539 frequency  $\langle f_{\text{DS}} \rangle_{\Delta t}$  (grey star) with the error bars corresponding to the variability  $\sigma_{f_{\text{DS}}}$   
 540 for each of the selected events. For all the events,  $f_{\text{obs}}$  lies in the variability range of  $\sigma_{f_{\text{DS}}}$   
 541 so that the Doppler shifted frequency is close to zero and the fluctuations can be con-  
 542 sidered as non-propagating. An exception is event #4 since  $f_{\text{obs}}$  lies outside (but still very  
 543 close to) the variability range of  $f_{\text{DS}}$ . We still include event #4 in the list of EF events  
 544 as the other characteristics of the observed waves are consistent with the EF mode. Also,  
 545 it is worth clarifying that the so-called  $f_{\text{DS}}$  variability range,  $\sigma_{f_{\text{DS}}}$ , does not have to be  
 546 interpreted as a rigorously defined error of  $f_{\text{DS}}$ , but rather a qualitative estimation of the  
 547 uncertainty. The same quantities shown in Fig.10(a), this time normalized by the lower-  
 548 hybrid frequency  $f_{\text{LH}}$ , are shown in Fig.10(b). In all the events, the observed frequency  
 549 is comparable with the local  $f_{\text{LH}}$ . Fig.10(c)–(f) show other characteristics that we take  
 550 into account for the wave analysis in Sec.5. In all the events, the wave characteristics are  
 551 quite similar. Notably,  $k\rho_e$  ranges between 0.30 and 0.74 (Fig.10(c));  $\theta_{k_B}$  ranges between  
 552  $32^\circ$  and  $81^\circ$  indicating that the observed mode is oblique (Fig.10(d));  $\langle \mathcal{E}_{\text{long}} \rangle_{\Delta t, \Delta f}$  ranges  
 553 between 0.23 and 0.57 meaning that the observed waves have a significant electromag-  
 554 netic component (Fig.10(e)). The parameter  $\langle \zeta_e^\pm \rangle_{\Delta t}$  has a minimum value of 0.9 for event  
 555 #4 and a maximum of 2.4 for event #7 (Fig.10(f)). Another common feature of the fluc-  
 556 tuations observed in all the events is that all three  $\delta \mathbf{B}$  components have similar ampli-  
 557 tude (see Fig.5(b) and Fig.7(b) for event #6 and #7). Also, during all the events the  
 558 electron and ion velocity, notably in the GSM x direction, are large ( $|v_{e,x}| \gtrsim 800$  km/s  
 559 and  $|v_{i,x}| \gtrsim 500$  km/s, see Fig.2), indicating that all the intervals with EF waves and  
 560 where the EFI threshold is exceeded are located in the magnetic reconnection outflow  
 561 region.

562 We then compare the in situ observations of each event with the results of the nu-  
 563 merical solver PDRK, analogously to Sec.5 and 6 for event #6 and #7 (interval 7A). The  
 564 PDRK solver is run with initial parameters such as background magnetic field, density,  
 565 and temperatures, tailored to each event (see parameters in Table 1). For event #4, the  
 566 temperature anisotropy has been artificially increased in the solver by 23% (from the value  
 567  $T_{e,\parallel}/T_{e,\perp} = 1.10$  observed in situ to  $T_{e,\parallel}/T_{e,\perp} = 1.35$ ) in order to obtain an unsta-  
 568 ble EF mode. The fact that it is needed to consider a higher  $T_{e,\parallel}/T_{e,\perp}$  value to obtain  
 569 wave growth is not surprising as it is expected for the anisotropy to decrease as the in-  
 570 stability develops and the waves grow. Since waves are directly observed in situ, the elec-  
 571 tron temperature anisotropy at the time of the observations is likely lower than the  $T_{e,\parallel}/T_{e,\perp}$   
 572 at the time of the instability onset. For each event, we find a good agreement between  
 573 in situ observations and the model (not shown) suggesting that the waves observed in  
 574 the selected events are fluctuations generated by the EFI developing in the reconnection  
 575 outflow.

## 576 8 Discussion

577 In this study, we investigate a current sheet flapping event in the Earth's magne-  
 578 totail associated with strong flows in the x GSM direction indicative of ongoing magnetic  
 579 reconnection. The flow is directed tailward during the first part of the interval and Earth-  
 580 ward at the end of the interval, indicating that MMS observed a magnetic reconnection  
 581 X-line retreating tailward. Magnetic reconnection regions such as the outflow can be char-  
 582 acterized by strong temperature anisotropy so that temperature anisotropy-driven in-  
 583 stabilities, such as the EFI, can develop at those locations.

584 Even though the EFI has been invoked to explain the constrained electron tem-  
 585 perature anisotropy in a variety of plasma environments, direct observations of the EFI-  
 586 generated waves were lacking. In this study, we report in situ MMS observations of EF

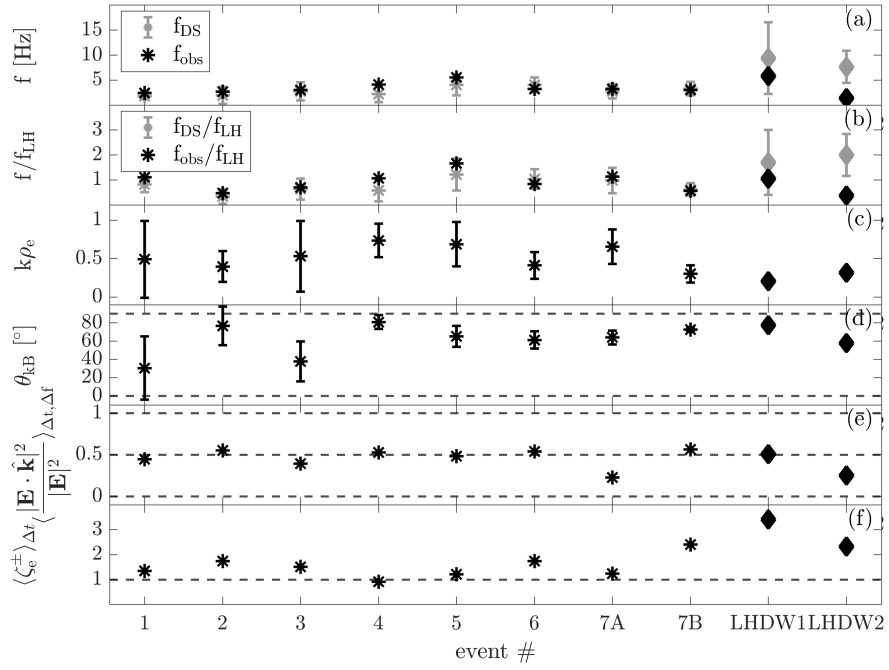


**Figure 10.** Fluctuations characteristics for the EF events (star markers) and two lower hybrid drift waves (LHDW) events observed in the magnetotail (diamond markers). Event LHDW1 and LHDW2 are reported respectively in (Chen et al., 2020) and (Cozzani et al., 2021). (a) Observed frequency  $f_{\text{obs}}$  and Doppler shift frequency averaged in the time interval of the fluctuations  $\langle f_{\text{DS}} \rangle_{\Delta t}$  with the associated uncertainty  $\sigma_{f_{\text{DS}}}$ . (b) Same as (a) but frequencies are normalized to  $f_{\text{LH}}$ . (c) Wave vector magnitude  $k\rho_e$ . (d)  $\theta_{\text{kB}}$ . (e)  $\langle \mathcal{E}_{\text{long}} \rangle_{\Delta t, \Delta f}$ . (f)  $\langle \zeta_e^{\pm} \rangle_{\Delta t}$ .

**Table 2.** Characteristics of the fluctuations of the EF events.  $\Delta t$  is the interval where the EF fluctuations are observed.

#	$\Delta t$ [UTC]	$f_{\text{obs}}$ [Hz]	$\langle f_{\text{DS}} \rangle_{\Delta t}$ [Hz]	$\sigma_{f_{\text{DS}}}$ [Hz]	$k\rho_e$	$\theta_{\text{kB}}$ [°]	$\langle \mathcal{E}_{\text{long}} \rangle_{\Delta t, \Delta f}$	$\langle \zeta_e^{\pm} \rangle_{\Delta t}$
1	15:25:03.0 – 15:25:04.6	2.4	1.8	0.7	0.49	32	0.45	1.3
2	15:28:24.6 – 15:28:27.2	2.7	1.9	1.7	0.40	77	0.55	1.7
3	15:28:51.4 – 15:28:53.8	3.0	2.7	1.8	0.53	38	0.39	1.5
4	15:30:58.5 – 15:31:01.5	4.1	2.2	1.7	0.74	81	0.53	0.9
5	15:31:41.9 – 15:31:42.7	5.5	4.0	2.1	0.69	65	0.48	1.2
6	15:38:08.0 – 15:38:11.0	3.2	4.0	1.5	0.41	61	0.54	1.7
7A	15:53:47.0 – 15:53:50.0	3.2	2.8	1.4	0.66	64	0.23	1.2
7B	15:53:50.5 – 15:53:53.0	3.0	3.3	1.3	0.30	73	0.57	2.4

587 waves in the reconnection outflow region. There are two distinct EF modes but, as spec-  
588 ified above, we focus exclusively on the non-propagating EF mode since it has a larger  
589 growth rate and a lower instability threshold with respect to the propagating EF mode.  
590 While being located in the reconnection outflow, MMS observes several time intervals  
591 during which the EFI threshold is exceeded ( $\mathcal{T}_{\text{EFI}} > 0$ ). Taking into account the selec-  
592 tion criteria discussed in Sec. 4, we finally select seven events that are characterized by  
593 both  $\mathcal{T}_{\text{EFI}} > 0$  and wave activity. We presented a detailed wave analysis of two of those  
594 events, showing that the observed wave characteristics are in agreement with the prop-  
595 erties of the non-propagating EF mode.

596 Even though the non-propagating EF mode has distinct characteristics, it shares  
597 a few properties with the electromagnetic part of the lower hybrid mode. Lower hybrid  
598 drift waves (LHDW) are commonly observed in plasma regions characterized by strong  
599 spatial gradients in various quantities such as the density or the magnetic field. For ex-  
600 ample, the characteristics of the LHDW have been thoroughly investigated at the Earth's  
601 magnetopause (e.g., Graham et al., 2019). In the context of a current sheet, LHDW can  
602 be triggered by the lower hybrid drift wave instability (LHDI) and while an electrostatic,  
603 short wavelength ( $k\rho_e \sim 1$ ) mode will be localized at the edges of the current sheet, an  
604 electromagnetic, longer wavelength ( $k\sqrt{\rho_e\rho_i} \sim 1$ ) mode can be present at the center (Yoon  
605 et al., 2002; Daughton, 2003). The electrostatic mode is characterized by a larger growth  
606 rate but it stays confined at the edges of the current sheet, while the electromagnetic mode  
607 develops at later times and is present at the current sheet center (Daughton, 2003). The  
608 electromagnetic LHD mode is characterized by oblique propagation with respect to the  
609 background magnetic field and by frequency of the order of the lower hybrid frequency  
610  $f_{\text{LH}}$ . So, both the electromagnetic LHD mode and the non-propagating EF mode are elec-  
611 tromagnetic and characterized by large wave-normal angles. Despite these similarities,  
612 the two modes are of course distinct. Firstly, the EF mode is non-propagating so it has

613 zero real frequency, while LHDW have a frequency of the order of  $f_{\text{LH}}$ . Also, EFI-generated  
 614 waves are expected to have a quite low  $\delta B_{\parallel}/\delta B$ , while for obliquely propagating LHDW  
 615  $\delta B_{\parallel}$  is the largest component of the fluctuating magnetic field.

616 To further corroborate our results, we make sure that the fluctuations that we have  
 617 identified as the EF waves are not the electromagnetic lower hybrid mode, which has been  
 618 reported in several studies investigating magnetic reconnection in the Earth's magne-  
 619 totail and at the magnetopause (Chen et al., 2020; Cozzani et al., 2021; Wang et al., 2022;  
 620 Yoo et al., 2020). This further check is motivated by the fact that the observations are  
 621 complex and characterized by significant uncertainties. The direct comparison with the  
 622 LHD mode – which shares characteristics with the EF waves – will demonstrate that we  
 623 are not mislabeling the observed waves and provide further robustness to our results. Thus,  
 624 we will consider two LHDW events corresponding to reconnection electron diffusion re-  
 625 gion (EDR) crossings in the magnetotail reported by Cozzani et al. (2021) (on 2017-08-  
 626 10 at 12:18:33.0) and Chen et al. (2020) (on 2017-07-03 at 05:27:07.5). As for the seven  
 627 events discussed in previous sections, we computed the EFI threshold and we performed  
 628 the wave analysis. The results are summarized in Fig. 10 (diamond markers), where the  
 629 event reported in Chen et al. (2020) is labeled as event LHDW1 ( $\Delta t = 05:27:07.15\text{--}05:27:07.75$   
 630 on 2017-07-03) and the event reported in Cozzani et al. (2021) is labeled as LHDW2 ( $\Delta t =$   
 631  $12:18:30.30\text{--}12:18:36.50$ ,  $\Delta \mathcal{T}_{\text{EFI}>0} = 12:18:32.07\text{--}12:18:33.54$  on 2017-08-10). We note that  
 632 while the EFI threshold is reached during event LHDW2, it is never reached for LHDW1,  
 633 neither during the interval of wave activity nor considering an interval of several seconds  
 634 centered around the interval of wave activity. For this reason, we could not define  $\Delta \mathcal{T}_{\text{EFI}>0}$   
 635 for event LHDW1. Both events present characteristics that are similar to the EF events  
 636 ( $k\rho_e \lesssim 1$ , oblique  $\theta_{\text{kB}}$  and  $\mathcal{E}_{\text{long}} \lesssim 0.5$ ). However, for LHDW2 we observe a non-zero  
 637 frequency (see Fig. 10(a) and (b)), so the observed waves could not be identified as non-  
 638 propagating EF waves. Concerning event LHDW1, while the observed frequency (black  
 639 diamond in Fig. 10(a) and (b)) lies inside the variability range  $\sigma_{f_{\text{DS}}}$ , we note that  $\sigma_{f_{\text{DS}}}$   
 640 is at least four times larger than any  $\sigma_{f_{\text{DS}}}$  computed for the EF events, indicating that  
 641 the measurement is not reliable in this case. Also, the behavior of  $f_{\text{DS}}$  is drastically dif-  
 642 ferent in LHDW1 and the EF events. During the EF events, we observe the Doppler shift  
 643 frequency  $f_{\text{DS}}$  fluctuating around the value of the observed frequency  $f_{\text{obs}}$  so that for sev-  
 644 eral points in the time interval with wave activity  $f_{\text{DS}} = f_{\text{obs}}$  (see e.g. Fig.7(c)). In con-  
 645 trast, during the wave activity interval of event LHDW1,  $f_{\text{DS}}$  does not fluctuate around  
 646  $f_{\text{obs}}$  (not shown); it varies approximately linearly during the considered interval and it  
 647 takes the value  $f_{\text{obs}}$  only twice. More importantly, the EFI instability threshold is never  
 648 exceeded during event LHDW1. Hence, it is unlikely that EFI-generated waves would  
 649 be observed during event LHDW1. We conclude that, while the observed EF and LHDW  
 650 waves share some similarities, it is possible to distinguish between the two modes. This  
 651 comparison further confirms that the reported events are reliably identified as EF fluc-  
 652 tuations.

653 As mentioned in previous sections, during several of the EF events, the waves that  
 654 we have identified as EFI-generated are not observed in correspondence of the EF un-  
 655 stable intervals where  $\mathcal{T}_{\text{EFI}} > 0$ , but rather immediately before or after. This may be  
 656 unexpected as we might expect to observe the EF waves in the source region, as they  
 657 are non-propagating fluctuations. At the same time, we expect the electron temperature  
 658 anisotropy to decrease as the waves grow and the instability proceeds to the non-linear  
 659 stage leading to electron isotropization. This means that MMS could observe a region  
 660 with unstable plasma without (prior to) wave development and observe clear wave ac-  
 661 tivity in a region where the instability has already saturated and reduced the anisotropy  
 662 of the plasma, so it is stable to EFI at the time of the observations.

663 The validity of this interpretation depends on the time scales associated with the  
 664 development and saturation of EFI compared to the duration of the observed intervals  
 665 with  $\mathcal{T}_{\text{EFI}} > 0$  and of the intervals with wave activity. The time scales of interest are

666 related to the wave growth rate  $\gamma$ ,  $T_\gamma = 2\pi/\gamma$  and to the time required to reach the  
 667 maximum fluctuations amplitude  $T_{\text{peak}}$ . These two quantities cannot be easily computed  
 668 with in situ measurements. However, we can obtain an estimation of  $T_\gamma$  from the results  
 669 of the linear solver. The time scale  $T_{\text{peak}}$  has been evaluated in simulation studies. The  
 670 value of  $T_{\text{peak}}$  is quite similar in simulation studies by Gary and Nishimura (2003); Cam-  
 671 poreale and Burgess (2008); Hellinger et al. (2014) and corresponds to  $T_{\text{peak}} \approx 5-10 T_{\gamma_{\text{max}}}$ ,  
 672 where  $T_{\gamma_{\text{max}}} = 2\pi/\gamma_{\text{max}}$  is computed for the maximum growth rate. In the case of event  
 673 #6, the interval where the EFI threshold is exceeded,  $\Delta t_{\mathcal{T}_{\text{EFI}} > 0}$ , has a duration of 0.49  
 674 s. The maximum growth rate is  $\gamma_{\text{max}} = 0.025 \Omega_{\text{ce}}$  (see Fig.8(a)) so that  $T_{\gamma_{\text{max}}} = 2\pi/\gamma_{\text{max}} =$   
 675 0.43 s (here  $\Omega_{\text{ce}} = 580$  rad/s for a background magnetic field of 3 nT). Considering the  
 676 estimate value of  $T_{\text{peak}}$  based on simulations results,  $T_{\text{peak}} \approx 5 - 10 T_{\gamma_{\text{max}}} \approx 2.15 -$   
 677 4.3 s. Hence,  $T_{\text{peak}} = 4.4-8.7 \Delta t_{\mathcal{T}_{\text{EFI}} > 0}$ , meaning that the time spent by MMS in the  
 678 unstable region is not enough to observe the wave development. At the same time, it is  
 679 not surprising that the waves remain in the region where the temperature anisotropy is  
 680 already being reduced, as the waves are non-propagating. This estimation yields to sim-  
 681 ilar results also for the other events that have the wave activity not co-located with  $\Delta t_{\mathcal{T}_{\text{EFI}} > 0}$ .  
 682 This simple qualitative estimation, despite its inherent limitations, can help us under-  
 683 stand the lack of wave observations in the intervals with  $\mathcal{T}_{\text{EFI}} > 0$ .

684 The observed EF fluctuations are located in the reconnection outflow, which is char-  
 685 acterized by strong flow. It is worth underlining that the presence of this strong elec-  
 686 tron flow is crucial for observing the non-propagating EF mode as it allows for a signif-  
 687 icant Doppler shift frequency that, in the case of non-propagating modes, will coincide  
 688 with the observed frequency ( $f_{\text{obs}} = f_{\text{DS}} \pm \sigma_{f_{\text{DS}}}$ ). We note, however, that a non-negligible  
 689 Doppler shift frequency depends not only upon the magnitude of  $\mathbf{v}_e$  but also on the an-  
 690 gle between  $\mathbf{v}_e$  and  $\mathbf{k}$ . In all considered events,  $\mathbf{v}_e$  has a significant component along the  
 691 wave vector yielding significant Doppler shift frequency.

692 Interestingly, for all the EF events the observed waves are more complex than pre-  
 693 dicted by linear dispersion theory. The observed EF waves exhibit magnetic field fluc-  
 694 tuations of similar amplitude for all three components in both GSM and field-aligned  
 695 (FAC) coordinate systems (see Fig.4(b) and Fig.5(b) for event #6; Fig.6(b) and Fig.7(b)  
 696 for event #7). This is in contrast with the linear theory predicting low  $\delta B_{\parallel}/\delta B$ , mean-  
 697 ing that the components perpendicular to the background magnetic field are dominat-  
 698 ing the fluctuations (see Fig.1(d) and Fig.8(c), 9(c)). Also, while all the observed waves  
 699 have a clear electromagnetic component, for several events  $\langle \mathcal{E}_{\text{long}} \rangle_{\Delta t, \Delta f} \sim 0.5$  further  
 700 indicating that the observed waves are quite complex as they are not fully electromag-  
 701 netic or electrostatic.

## 702 9 Conclusions

703 We used high-resolution in situ measurements by MMS to investigate EFI-generated  
 704 fluctuations in the outflow region of magnetic reconnection. We considered a current sheet  
 705 flapping event in the Earth's magnetotail when MMS was almost continuously measur-  
 706 ing the reconnection exhaust (both tailward and Earthward flow). We identified seven  
 707 events characterized by wave activity during which the EFI threshold is exceeded.

708 Our results show that the observed waves have properties consistent with the non-  
 709 propagating EF mode as predicted by the linear kinetic dispersion theory. In particu-  
 710 lar, we observe non-propagating fluctuations (i.e. zero real frequency) characterized by  
 711 a wave vector  $k\rho_e \lesssim 1$  directed obliquely with respect to the background magnetic field,  
 712 with significant electromagnetic component and resonant with electrons. However, there  
 713 are also some differences between the observed fluctuations and the prediction of the lin-  
 714 ear theory. Notably, all three fluctuating magnetic field components have similar am-  
 715 plitude; the waves are not fully electromagnetic or electrostatic, i.e.  $\langle \mathcal{E}_{\text{long}} \rangle_{\Delta t, \Delta f} \sim 0.5$ .

716 The investigation of the EF modes in the reconnection outflow region is crucial to  
 717 improve our knowledge of the global energy conversion associated with reconnection. In-  
 718 deed, the EFI-generated fluctuations are likely to lead to particle scattering and enhanced  
 719 wave-particle interaction which in turn can affect particle energization and energy con-  
 720 version during reconnection, ultimately altering the global energy budget of the mag-  
 721 netic reconnection process. This study, reporting for the first time direct observations  
 722 of the EFI-generated fluctuations, represents the first step toward a more complete un-  
 723 derstanding of the EFI and its possible interplay with reconnection.

724 The results of this work are also beneficial to the study of the EFI in other plasma  
 725 environments and regimes. In particular, the EFI is thought to play a key role in elec-  
 726 tron distribution isotropization in the solar wind but direct observation of the EF mode  
 727 is currently prevented by the limited time resolution of particle measurements and lack  
 728 of multi-spacecraft observations.

## 729 Open Research: Data Availability Statement

730 MMS data are available at <https://lasp.colorado.edu/mms/sdc/public/data/>  
 731 following the directories: `mms#/fgm/brst/l2` for FGM data, `mms#/edp/brst/l2` for EDP  
 732 data, `mms#/fpi/brst/l2/dis-dist` for FPI ion distributions, `mms#/fpi/brst/l2/dis-moms`  
 733 for FPI ion moments, `mms#/fpi/brst/l2/des-dist` for FPI electron distributions, and `mms#/fpi/brst/l2/des-`  
 734 `moms` for FPI electron moments. Data analysis was performed using the IRFU-Matlab  
 735 analysis package, available at <https://github.com/irfu/irfu-matlab>. The PDRK nu-  
 736 merical solver code is available at <https://github.com/hsxie/pdrk>.

## 737 Acknowledgments

738 The authors thank the entire MMS team and instruments' principal investigators for data  
 739 access and support. Thank you to Konrad Steinvall for helpful discussions. GC is sup-  
 740 ported by the European Research Council Consolidator grant 682068-PRESTISSIMO.  
 741 DBG is supported by the Swedish National Space Agency (SNSA), grant 128/17.

## 742 References

- 743 Biskamp, D. (2000). *Magnetic reconnection in plasmas*. Cambridge University Press.  
 744 doi: 10.1017/CBO9780511599958
- 745 Burch, J., Moore, T., Torbert, R., & Giles, B. (2016, 05). Magnetospheric multi-  
 746 scale overview and science objectives. *Space Science Reviews*, 199, 5-21. doi:  
 747 10.1007/s11214-015-0164-9
- 748 Camporeale, E., & Burgess, D. (2008). Electron firehose instability: Kinetic linear  
 749 theory and two-dimensional particle-in-cell simulations. *Journal of Geo-*  
 750 *physical Research: Space Physics*, 113(A7). doi: [https://doi.org/10.1029/](https://doi.org/10.1029/2008JA013043)  
 751 2008JA013043
- 752 Cattell, C., Breneman, A., Dombeck, J., Hanson, E., Johnson, M., Halekas, J., ...  
 753 Whittlesey, P. (2022, jan). Parker solar probe evidence for the absence of  
 754 whistlers close to the sun to scatter strahl and to regulate heat flux. *The*  
 755 *Astrophysical Journal Letters*, 924(2), L33. doi: 10.3847/2041-8213/ac4015
- 756 Chen, L.-J., Wang, S., Le Contel, O., Rager, A., Hesse, M., Drake, J., ... Avannov,  
 757 L. (2020, Jul). Lower-hybrid drift waves driving electron nongyrotropic heating  
 758 and vortical flows in a magnetic reconnection layer. *Phys. Rev. Lett.*, 125,  
 759 025103. doi: 10.1103/PhysRevLett.125.025103
- 760 Chew, G. F., Goldberger, M. L., Low, F. E., & Chandrasekhar, S. (1956). The  
 761 boltzmann equation and the one-fluid hydromagnetic equations in the ab-  
 762 sence of particle collisions. *Proceedings of the Royal Society of London.*  
 763 *Series A. Mathematical and Physical Sciences*, 236(1204), 112-118. doi:

- 764 10.1098/rspa.1956.0116
- 765 Cozzani, G., Khotyaintsev, Y. V., Graham, D. B., Egedal, J., André, M., Vaivads,  
766 A., . . . Burch, J. L. (2021, Nov). Structure of a perturbed magnetic reconnection  
767 electron diffusion region in the earth's magnetotail. *Phys. Rev. Lett.*, *127*,  
768 215101. doi: 10.1103/PhysRevLett.127.215101
- 769 Daughton, W. (2003). Electromagnetic properties of the lower-hybrid drift instability  
770 in a thin current sheet. *Physics of Plasmas*, *10*(8), 3103-3119. doi: 10  
771 .1063/1.1594724
- 772 Egedal, J., Le, A., & Daughton, W. (2013). A review of pressure anisotropy caused  
773 by electron trapping in collisionless plasma, and its implications for magnetic  
774 reconnection. *Physics of Plasmas*, *20*(6), 061201. doi: 10.1063/1.4811092
- 775 Ergun, R. E., Tucker, S., Westfall, J., Goodrich, K. A., Malaspina, D. M., Summers,  
776 D., . . . Cully, C. M. (2016). The axial double probe and fields signal  
777 processing for the mms mission. *Space Science Reviews*, *199*, 167-188. doi:  
778 10.1007/s11214-014-0115-x
- 779 Feldman, W. C., Asbridge, J. R., Bame, S. J., Montgomery, M. D., & Gary, S. P.  
780 (1975). Solar wind electrons. *Journal of Geophysical Research (1896-1977)*,  
781 *80*(31), 4181-4196. doi: <https://doi.org/10.1029/JA080i031p04181>
- 782 Gao, J. W., Rong, Z. J., Cai, Y. H., Lui, A. T. Y., Petrukovich, A. A., Shen, C.,  
783 . . . Wan, W. X. (2018). The distribution of two flapping types of mag-  
784 netotail current sheet: Implication for the flapping mechanism. *Jour-  
785 nal of Geophysical Research: Space Physics*, *123*(9), 7413-7423. doi:  
786 <https://doi.org/10.1029/2018JA025695>
- 787 Gary, S. P. (1993). *Theory of space plasma microinstabilities*. Cambridge University  
788 Press. doi: 10.1017/CBO9780511551512
- 789 Gary, S. P., Lavraud, B., Thomsen, M. F., Lefebvre, B., & Schwartz, S. J. (2005).  
790 Electron anisotropy constraint in the magnetosheath: Cluster observa-  
791 tions. *Geophysical Research Letters*, *32*(13). doi: [https://doi.org/10.1029/  
792 2005GL023234](https://doi.org/10.1029/2005GL023234)
- 793 Gary, S. P., & Madland, C. D. (1985). Electromagnetic electron temperature  
794 anisotropy instabilities. *Journal of Geophysical Research: Space Physics*,  
795 *90*(A8), 7607-7610. doi: <https://doi.org/10.1029/JA090iA08p07607>
- 796 Gary, S. P., & Nishimura, K. (2003). Resonant electron firehose instability: Particle-  
797 in-cell simulations. *Physics of Plasmas*, *10*(9), 3571-3576. doi: 10.1063/1  
798 .1590982
- 799 Gary, S. P., Smith, C. W., Lee, M. A., Goldstein, M. L., & Forslund, D. W. (1984).  
800 Electromagnetic ion beam instabilities. *The Physics of Fluids*, *27*(7), 1852-  
801 1862. doi: 10.1063/1.864797
- 802 Graham, D. B., Khotyaintsev, Y. V., Norgren, C., Vaivads, A., André, M., Drake,  
803 J. F., . . . Ergun, R. E. (2019). Universality of lower hybrid waves at earth's  
804 magnetopause. *Journal of Geophysical Research: Space Physics*, *124*(11),  
805 8727-8760. doi: <https://doi.org/10.1029/2019JA027155>
- 806 Graham, D. B., Khotyaintsev, Y. V., Vaivads, A., & André, M. (2016). Electro-  
807 static solitary waves and electrostatic waves at the magnetopause. *Journal of  
808 Geophysical Research: Space Physics*, *121*(4), 3069-3092. doi: [https://doi.org/  
809 10.1002/2015JA021527](https://doi.org/10.1002/2015JA021527)
- 810 Hellinger, P., Trávníček, P. M., Decyk, V. K., & Schriver, D. (2014). Oblique  
811 electron fire hose instability: Particle-in-cell simulations. *Journal of Geophys-  
812 ical Research: Space Physics*, *119*(1), 59-68. doi: [https://doi.org/10.1002/  
813 2013JA019227](https://doi.org/10.1002/2013JA019227)
- 814 Hollweg, J. V., & Völk, H. J. (1970). New plasma instabilities in the solar wind.  
815 *Journal of Geophysical Research (1896-1977)*, *75*(28), 5297-5309. doi: [https://  
816 doi.org/10.1029/JA075i028p05297](https://doi.org/10.1029/JA075i028p05297)
- 817 Innocenti, M. E., Tenerani, A., Boella, E., & Velli, M. (2019, sep). Onset and  
818 evolution of the oblique, resonant electron firehose instability in the ex-

- 819           panding solar wind plasma. *The Astrophysical Journal*, 883(2), 146. doi:  
820           10.3847/1538-4357/ab3e40
- 821 Lazar, M., Shaaban, S. M., Poedts, S., & Š. Štverák. (2016). Firehose constraints of  
822           the bi-kappa-distributed electrons: a zero-order approach for the suprathermal  
823           electrons in the solar wind. *Monthly Notices of the Royal Astronomical Society*,  
824           464(1), 564–571. doi: <https://doi.org/10.1093/mnras/stw2336>
- 825 Le, A., Stanier, A., Daughton, W., Ng, J., Egedal, J., Nystrom, W. D., & Bird,  
826           R. (2019). Three-dimensional stability of current sheets supported by  
827           electron pressure anisotropy. *Physics of Plasmas*, 26(10), 102114. doi:  
828           10.1063/1.5125014
- 829 Leonenko, M. V., Grigorenko, E. E., Zelenyi, L. M., Malova, H. V., Malykhin,  
830           A. Y., Popov, V. Y., & Büchner, J. (2021). Mms observations of su-  
831           per thin electron-scale current sheets in the earth’s magnetotail. *Journal*  
832           *of Geophysical Research: Space Physics*, 126(11), e2021JA029641. doi:  
833           <https://doi.org/10.1029/2021JA029641>
- 834 Li, X., & Habbal, S. R. (2000). Electron kinetic firehose instability. *Journal of*  
835           *Geophysical Research: Space Physics*, 105(A12), 27377-27385. doi: [https://doi](https://doi.org/10.1029/2000JA000063)  
836           .[org/10.1029/2000JA000063](https://doi.org/10.1029/2000JA000063)
- 837 Lindqvist, P.-A., Olsson, G., Torbert, R., King, B., Granoff, M., Rau, D., ...  
838           Tucker, S. (2016). The spin-plane double probe electric field instrument for  
839           mms. *Space Science Reviews*, 199, 137–165. doi: 10.1007/s11214-014-0116-9
- 840 López, R. A., Micera, A., Lazar, M., Poedts, S., Lapenta, G., Zhukov, A. N., ...  
841           Shaaban, S. M. (2022, may). Mixing the solar wind proton and electron  
842           scales. theory and 2d-PIC simulations of firehose instability. *The Astrophysical*  
843           *Journal*, 930(2), 158. doi: 10.3847/1538-4357/ac66e4
- 844 Maneva, Y., Lazar, M., Viñas, A., & Poedts, S. (2016, nov). MIXING THE SO-  
845           LAR WIND PROTON AND ELECTRON SCALES: EFFECTS OF ELEC-  
846           TRON TEMPERATURE ANISOTROPY ON THE OBLIQUE PROTON  
847           FIREHOSE INSTABILITY. *The Astrophysical Journal*, 832(1), 64. doi:  
848           10.3847/0004-637x/832/1/64
- 849 Messmer, P. (2002). Temperature isotropization in solar flare plasmas due to the  
850           electron firehose instability. *A&A*, 382(1), 301-311. doi: 10.1051/0004-6361:  
851           20011583
- 852 Paesold, G., & Benz, A. O. (2003). Test particle simulation of the electron firehose  
853           instability. *A&A*, 401(2), 711-720. doi: 10.1051/0004-6361:20030113
- 854 Pilipp, W., & Völk, H. J. (1971). Analysis of electromagnetic instabilities parallel  
855           to the magnetic field. *Journal of Plasma Physics*, 6(1), 1–17. doi: 10.1017/  
856           S0022377800025654
- 857 Pilipp, W. G., Miggenrieder, H., Montgomery, M. D., Mühlhäuser, K. H., Rosen-  
858           bauer, H., & Schwenn, R. (1987). Characteristics of electron velocity distri-  
859           bution functions in the solar wind derived from the helios plasma experiment.  
860           *Journal of Geophysical Research: Space Physics*, 92(A2), 1075-1092. doi:  
861           <https://doi.org/10.1029/JA092iA02p01075>
- 862 Pollock, C. J., Moore, T. E., Jacques, A. D., Burch, J. L., Gliese, U., Saito, Y., ...  
863           Zeuch, M. A. (2016). Fast plasma investigation for magnetospheric multiscale.  
864           *Space Science Reviews*, 199, 331-406. doi: 10.1007/s11214-016-0245-4
- 865 Richard, L., Khotyaintsev, Y. V., Graham, D. B., Sitnov, M. I., Le Contel, O.,  
866           & Lindqvist, P.-A. (2021). Observations of short-period ion-scale current  
867           sheet flapping. *Journal of Geophysical Research: Space Physics*, 126(8),  
868           e2021JA029152. doi: <https://doi.org/10.1029/2021JA029152>
- 869 Russell, C. T., Anderson, B. J., Baumjohann, W., Bromund, K. R., Dearborn, D.,  
870           Fischer, D., ... Richter, I. (2016). The magnetospheric multiscale magnetome-  
871           ters. *Space Science Reviews*, 199, 189-256. doi: 10.1007/s11214-014-0057-3
- 872 Shaaban, S. M., Lazar, M., López, R. A., Yoon, P. H., & Poedts, S. (2021).  
873           Advanced interpretation of waves and instabilities in space plasmas. In

- 874 M. Lazar & H. Fichtner (Eds.), *Kappa distributions: From observational*  
 875 *evidences via controversial predictions to a consistent theory of nonequilib-*  
 876 *rium plasmas* (pp. 185–218). Cham: Springer International Publishing. doi:  
 877 10.1007/978-3-030-82623-9\_10
- 878 Shaaban, S. M., Lazar, M., López, R. A., Fichtner, H., & Poedts, S. (2019, mar).  
 879 Firehose instabilities triggered by the solar wind suprathermal electrons.  
 880 *Monthly Notices of the Royal Astronomical Society*, *483*(4), 5642–5648. doi:  
 881 10.1093/mnras/sty3377
- 882 Verscharen, D., Chandran, B. D. G., Boella, E., Halekas, J., Innocenti, M. E., Ja-  
 883 garlamudi, V. K., . . . Whittlesey, P. L. (2022). Electron-driven instabili-  
 884 ties in the solar wind. *Frontiers in Astronomy and Space Sciences*, *9*. doi:  
 885 10.3389/fspas.2022.951628
- 886 Štverák, v., Trávníček, P., Maksimovic, M., Marsch, E., Fazakerley, A. N., &  
 887 Scime, E. E. (2008). Electron temperature anisotropy constraints in the  
 888 solar wind. *Journal of Geophysical Research: Space Physics*, *113*(A3). doi:  
 889 <https://doi.org/10.1029/2007JA012733>
- 890 Wang, S., Chen, L.-J., Bessho, N., Ng, J., Hesse, M., Graham, D. B., . . . Giles, B.  
 891 (2022). Lower-hybrid wave structures and interactions with electrons observed  
 892 in magnetotail reconnection diffusion regions. *Journal of Geophysical Research:*  
 893 *Space Physics*, *127*(5), e2021JA030109. (e2021JA030109 2021JA030109) doi:  
 894 <https://doi.org/10.1029/2021JA030109>
- 895 Xie, H., & Xiao, Y. (2016). PDRK: A general kinetic dispersion relation solver for  
 896 magnetized plasma. *Plasma Science and Technology*, *18*(2), 97–107. doi: 10  
 897 .1088/1009-0630/18/2/01
- 898 Yoo, J., Ji, J.-Y., Ambat, M. V., Wang, S., Ji, H., Lo, J., . . . Goodman, A. (2020).  
 899 Lower hybrid drift waves during guide field reconnection. *Geophysical Research*  
 900 *Letters*, *47*(21), e2020GL087192. doi: <https://doi.org/10.1029/2020GL087192>
- 901 Yoon, P. H., Lui, A. T. Y., & Sitnov, M. I. (2002). Generalized lower-hybrid drift  
 902 instabilities in current-sheet equilibrium. *Physics of Plasmas*, *9*(5), 1526–1538.  
 903 doi: 10.1063/1.1466822
- 904 Zhang, X., Angelopoulos, V., Artemyev, A. V., & Liu, J. (2018). Whistler and  
 905 electron firehose instability control of electron distributions in and around  
 906 dipolarizing flux bundles. *Geophysical Research Letters*, *45*(18), 9380–9389.  
 907 doi: <https://doi.org/10.1029/2018GL079613>